Experimental Mechanics (2024) 64:655–674
https://doi.org/10.1007/s11340-024-01050-4

RESEARCH PAPER

An Exploration of Grain-Averaged Stress Measurement Using Partial Unloads with *In situ* Microscopic Image Correlation

O. Türkoğlu[1] · **C.C. Aydıner**[1]

Received: 11 September 2023 / Accepted: 22 February 2024 / Published online: 20 March 2024
© The Author(s) 2024

Abstract

Background In polycrystal mechanics, determination of stress is associated with diffraction methods that measure (the inherently-related) elastic strain. Microscopic digital image correlation (DIC), while commanding much higher intragranular resolution, measures total strain, and its local accuracy is typically insufficient to evaluate elastic strain magnitudes.

Objective *In situ* DIC measurements over a partial unload of the polycrystal, where strains are virtually elastic, are explored for grain-averaged elastic strains and then, through a posed formalism, the stresses at the point of unload. Grain averaging is functionally employed to improve the DIC accuracy. The large objective is to emulate *in situ* complementary diffraction.

Methods Nickel with high elastic anisotropy is chosen. The utilized highly-automated instrument offers maximal resolution for DIC with optical microscopy over a gross grain field. Orientations are predetermined for the same grain layer via electron backscatter diffraction. High-accuracy grain masks are produced to isolate the strain fields of individual grains.

Results Very promising results are shown over a number of grains with sensible apparent compliance and stress values as well as linear unload behavior. Grains with sane results are largely predicted by a posed objectivity test that relies on DIC repeated with multiple reference loads.

Conclusion Though it will require extremely careful implementations of microscopic DIC with high *intragranular* resolution, the premise of measuring *intergranular* stress fields via partial unloads seems to be viable and worthy of further exploration and verification. This capability that is superposed over strain measurement offers a more stringent validation of high-fidelity crystal plasticity models.

Keywords Digital image correlation · Optical microscopy · Grain-resolved stress measurement · Face centered cubic

Introduction

Digital image correlation (DIC) has become the standard technique for measuring strain fields in industry and academia. The method has no innate length scale, and its microscopy applications (micro-DIC) have also been predominant among micro-scale strain mapping techniques [1, 2]. Micro-DIC allows comprehensive measurements of material deformation with high spatial resolution and statistical significance [2–5]. These findings have been particularly significant for the mechanics of polycrystalline aggregates (polycrystals). Multi-scale strain patterning [4, 6] that is inherent to a deforming polycrystal can now be detailed by micro-DIC, offering validation for novel models that seek high fidelity at the crystallite scale [7–10].

To date, *in situ* diffraction measurements have been carrying a principal load in validating crystal plasticity models [11–14]. With the classification of mechanical fields as type-I (macroscopic/aggregate-average), type-II (intergranular), and type-III (intragranular), most diffraction measurements can be designated type-II, with the common bulk diffraction rather resolved over crystallographic-orientation families [11, 15] (strain for each pole *hkl* corresponds to an average over sparsely-distributed grains in the diffraction volume that obey a common diffraction condition). More specialized methods can offer single-grain-resolved (grain-averaged) type-II results [16–18]. While type-III diffraction

C. C. Aydıner is a member of SEM.

✉ C.C. Aydıner
can.aydiner@boun.edu.tr

O. Türkoğlu
olcay.turkoglu@boun.edu.tr

[1] Mechanical Engineering Department, Boğaziçi University, Bebek, Istanbul 34342, Turkey

measurements [19–21] exist, varying degrees of type-III resolution is more achievable and typical with micro-DIC [4, 5, 22–24]. Note, as a fundamental distinction, diffraction measures lattice strain whereas DIC measures total strain. (Though not an exception to this fact, duly note the idea of Stinville et al. [25] to distinguish elastic and plastic strain fields by *localization degree* in ultra-high-resolution DIC that resolves slip traces.) Lattice strain is deemed equivalent to elastic strain that is inherently linked to the stress felt by the material, though whether stress components can be formalized over a consistent material region [18] depends on the type of diffraction measurement.

When micro-DIC—well established in detailing local plasticity over a polycrystal—is assessed for elastic strain measurement with an eye on stress deduction, two impediments are clear: (i) While diffraction intrinsically measures elastic strain, DIC can only measure elastic strain when it is (virtually) equal to the total strain, and (ii) typical local strain sensitivity of DIC (around 10^{-3}) is insufficient to identify elastic strains in most crystalline metals. Regarding the first, note, after a polycrystal is pushed into plasticity, strains over (partial) unloads seem to uniquely fit this description. For the second, we recognize that averaging of local fields can be used to improve the DIC accuracy at the cost of resolution.

In the scope of micro-DIC over a polycrystal where each grain is sampled with high intragranular resolution, one can then raise an important question. If grain-averaged strains are calculated, is the average sufficiently improved in accuracy to measure the average elastic strain components of a particular grain over an unload? If, further, stress components can be postulated from such measurements, a sharper premise arises: If one makes high-resolution type-III measurements of (total) strain with micro-DIC, can one estimate type-II (grain-averaged) stresses over the polycrystalline aggregate, imitating the role of complementary diffraction methods?

This study will explore this premise with a novel *in situ* DIC variant with area-scanning optical microscopy [6, 22] that achieves elevated intragranular resolution over mm-sized fields by employing high resolution [high numerical aperture (NA)] objectives, rendered possible automated corrective measures. A simple material is elected (FCC Nickel) but with high anisotropy ratio (=2.5) to promote intergranular differences that are to be observed and compared. The study further develops meticulous procedures for (i) incorporating orientation information from electron backscatter diffraction (EBSD), and (ii) forming accurate grain masks that are necessary to single out the strain fields of individual grains.

The *in situ* measurement capability is critically used to collect finely spaced data points over the unload, allowing a formal assessment of the linearity of grain-averaged strains with applied stress. Multiple data points are also used to improve the accuracy of the unloading slopes in axial, transverse and in-plane-shear strains via data fitting. Through these slopes, a stress estimate for each grain is postulated. Internal robustness measures for the results (e.g., picking DIC reference images at multiple load points, binary erosion of grain masks) are devised and tested. Further, two sets of accompanying model calculations (isostress and full-field spectral method) are utilized for comparison.

In sum, here, the idea of grain-resolved stress estimates using micro-DIC fields (over functionally employed unloads) is explored along with methodologies to check the viability and sanity of the results.

Material and Methods

A 99.5%-purity nickel rod with 6.35 mm diameter is procured from Alfa Aesar. It is heat treated (4 h at 750 °C) to increase the grain size (to 25 μm on average). A dog-bone specimen [26] with nominal 6 mm gage length, and $3.2 \times 3.2\,\text{mm}^2$ cross-section is extracted with wire electric discharge machining (EDM) along the extrusion direction (ED) of the rod. The sample is hot-mounted in bakelite and metallographically prepared using an automated grinding/polishing machine. With rough grinding (P800 at 50N load), a considerable thickness (200 μm) is first removed to eliminate any EDM layer, followed by gradual fine grinding (P1200-P4000) at 50 N. The specimen is then gently polished under minimal load (10 N) for 60 min using a colloidal silica solution.

Strategy for the Combined Implementation of EBSD and Microscopic DIC

While the polished surface can be utilized (without etching) for EBSD orientation mapping, the remaining procedure requires a careful consideration of the subsequent micro-DIC experiment and its analysis. It is crucial that (i) the layer of grains mapped by EBSD remains the same as those investigated with micro-DIC, and (ii) the grains in EBSD can be uniquely identified in the micro-DIC images for orientation assignment. The accuracy of the latter benefits immensely from revealing the grain boundaries by etching, but etching after EBSD would remove material and compromise the first.

Etching is therefore performed prior to EBSD here. To reveal grain boundaries while maintaining the surface quality/flatness for a successful EBSD measurement, an iterative procedure is devised: etching with a diluted (10%) Marble's reagent followed by 1 min polishing, repeated three times.

Fiducial markers are placed in the gage section with a micro-Vickers indenter to aid region identification [27].

Then, the sample is removed from the mold with cautious mechanical operations.

Next, EBSD is performed ("Electron Backscatter Diffraction" section), and the DIC pattern ("DIC Patterning" section) is introduced. To facilitate a unified presentation, Fig. 1(a) introduces the entire polycrystalline domain considered in this study with a stitched image of the micro-DIC field after patterning. Here, the sample is imaged inside the load frame but at zero-load (point "O").

Electron Backscatter Diffraction

EBSD is performed with an FEI Nova Nanosem 430 scanning electron microscope (SEM), equipped with EDAX EBSD. EBSD step size is 3 μm. Scanned fields are selected in accordance with the fiducial markers, two of which are marked with blue arrows in Fig. 1(a). Since the scans take long hours, multiple neighboring EBSD scans are conducted as a reliability measure. The material fields of Fig. 1(a) thus contains three EBSD scans in a horizontal row.

The central EBSD inverse pole figure map (*hkl* ||ED) that contains 1200 grains is provided in Fig. 1(b), with its 850×850 μm^2 domain marked in Fig. 1(a). The confidence index [28] is healthy (~ 0.7). Corresponding pole figures are shown in Fig. 1(f), presenting a mild texture with the typical 111 and 100 FCC wire texture components [29].

DIC Patterning

After EBSD but before patterning, an array of images (details in "Procedure of the *In situ* Micro-DIC Experiment" section) analogous to those stitched in Fig. 1(a) are recorded. For closer inspection, these pre-pattern images are compared to the patterned field after a two-tier zoom into Fig. 1(a), the first [orange box in Fig. 1(a)] shown in Fig. 1(c) and the second [blue box in Fig. 1(c)] shown in Fig. 1(d). Figure 1(e) is the corresponding region cropped from the pre-pattern images. The two grains marked in both Fig. 1(d) and (e) are also marked in Fig. 1(b). Note, Fig. 1(e) also represents the quality of the sample surface in the EBSD scans.

The DIC pattern is critical in the current study where minute strains are explored. Black paint speckles are applied with an airbrush not directly on the sample (unlike Refs. [2, 22, 30]), but to the sticky side of a residue-free tape (Micro-Measurements PCT-3 M) that is gently attached to the gage section and peeled back. With repetitions of this process, the desired speckle density is gradually attained in a highly homogeneous pattern.

Setup

The setup [22, 31], sketched in Fig. 2(a), comprises (i) a miniature 10 kN Kammrath & Weiss load frame, (ii) an *X*-*Y*-*Z* positioning array, and (iii) macroscopic (macro-DIC) and microscopic (micro-DIC) optical lines. The micro-DIC line comprises a FLIR camera (5 Megapixel, Sony IMX250 sensor), a Navitar Ultrazoom 6000 tube lens with bright-field LED illumination, and a Mitutoyo M Plan APO 20x long working distance (WD = 20 mm), high-resolution objective (numerical aperture, NA = 0.42). Figure 2(b) shows a cropped photo of the micro-DIC line over the load frame. Given the minuscule sample, the macro-DIC line also uses a low-powered microscope (Edmund Optics zoom inspection at 1x). The nominal field length per pixel for the micro- and macro-DIC lines are 0.0998 (virtually 0.1) and 5.67 μm/pixel, respectively. An in-house automation software manages the combined operation of the cameras and the positioners [22, 30].

Procedure of the *In situ* Micro-DIC Experiment

Load is incremented in position control under the macro-DIC line, where the macroscopic strains are calculated simultaneously. A macro-DIC image is shown in Fig. 2(c) at nominal 0.6% axial strain (load point "T"); after which the sample is unloaded in multiple steps. Macro-DIC axial strains are overlaid on the image, showing the lack of any considerable strain localization in the overall gage section. The micro-DIC domain [Fig. 1(a)] is indicated with a dashed box in Fig. 2(c). At selected loads, the sample is sent under the micro-DIC line to conduct an area scan (in *X*-*Y*) and record an array of overlapping 5 megapixel frames. Over Fig. 1(a), frames (1,1), (1,2), and (2,1) of the 7×13 array are symbolically marked. The stitching of this array into an approximately 300 megapixel image (1.2×2.7 mm^2) is performed in ImageJ [32, 33] through a python interface, where the merger coordinates are stored and later used for consistent data merger. The overall material field is chosen to envelop the EBSD data coverage with a safe margin. Field coordinates x_1-x_2 in μm are defined over Fig. 1(a); x_1-x_2 ticks will surround crops throughout the manuscript [e.g., Fig. 1(d)] to convey locality and scale.

The utilized high-NA objective has a minute depth of field (DOF = 1.6 μm), implying immediate defocusing under load if the images are straightforwardly recorded after planar (*X*-*Y*) adjustments. This setup employs high-resolution optics only thanks to its automated working distance correction in *Z*. Accordingly, at each load and at each frame (I,J), a *Z*-stack of images are recorded and analyzed for focus [34]. The sample is moved to the best focus point, Z_{foc}, before the DIC image is recorded for frame (I,J). This procedure maintains WD within a factor of DOF at each load/frame.

A material field correction [22] is also conducted at each load/frame. Here, the tentative image of a frame is compared with its counterpart in the previous load, and the overall shift

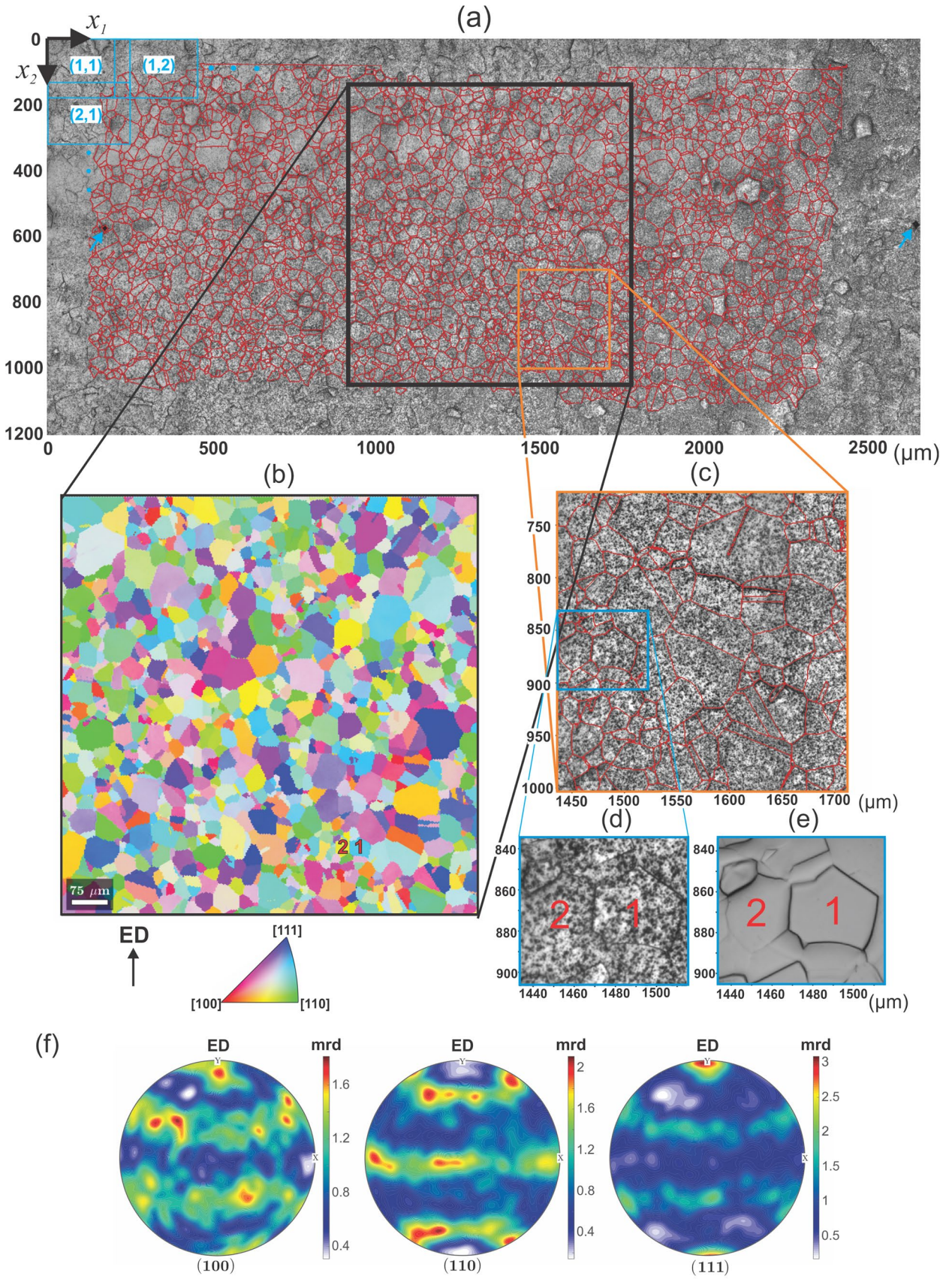
(a)
x_1
x_2
(1,1)
(1,2)
(2,1)
0
200
400
600
800
1000
1200
0
500
1000
1500
2000
2500 (μm)
(b)
(c)
750
800
850
900
950
1000
1450
1500
1550
1600
1650
1700 (μm)
(d)
(e)
840
860
880
900
1440
1460
1480
1500 (μm)
2 1
75 μm
ED
[111]
[100]
[110]
(f)
ED
mrd
1.6
1.2
0.8
0.4
(100)
2
1.6
1.2
0.8
0.4
(110)
3
2.5
2
1.5
1
0.5
(111)

◂**Fig. 1** (**a**) Stitched image of the full-field microscopic DIC scan overlaid the grain boundary network, (**b**) inverse pole figure map (*hkl* ‖ ED), (**c**) first-tier, (**d**) second-tier zoom out of the stitched image, (**e**) the zone in (**d**) before patterning, (**f**) pole figures (ED:extrusion direction, mrd:multiples of random)

in *X*-*Y* (rapidly calculated with FFT [35]) is compensated before recording the final image. Hence, the material field of each frame is maximally conserved (maximal avoidance of material flow to/from neighboring frames), allowing DIC among each frame [e.g., deformed (1,2) with respect to reference (1,2)] to suffice in producing continuous strain maps when the *data* is stitched.

Analysis

DIC Implementation

DIC is conducted with the subset-based inverse compositional algorithm [36] with first-order deformation mapping after a preliminary zeroth-order FFT analysis to get the initial values for displacements, u_1, u_2. 61×61 pixel subsets are used with 10 pixel grid/data spacing. The virtual 0.1 μm /pixel resolution yields a data spacing of 1 μm. Accordingly, the full-field micro-DIC analysis harbors $\sim 3 \times 10^6$ data points.

The displacement gradients $\partial u_i/\partial x_j$ are calculated from displacements using a 3×3 Savitzky-Golay differentiation kernel [37] with infinitesimal strains ε_{11}, ε_{22}, ε_{12} derived from these with their usual definition.

Micro-DIC strain uncertainty is determined from the standard deviation of strain fields after a rigid body motion [38], to be roughly $5\text{x}10^{-4}$ (500 $\mu\varepsilon$). This limited value attests to the quality of the speckle pattern and the resolution of the utilized microscopic optics in capturing the pattern.

Grain Mask

For a grain-resolved study of the mechanical fields, generating a grain mask (GM) is necessary, namely, a matrix (same size as the stitched image) composed of unique grain numbers that mark the domains of the grains. This mask is, first, painstakingly generated over the pre-pattern area scan, putting the stitched image in one layer of a photo-processing software and then drawing a spline network over the grain boundaries (GBs) on another layer. The formed GB network is also verified against the EBSD map and then converted to a GM with OpenCV [39]. This root GM is formed over the pre-pattern field, since the pattern occasionally conceals the GBs. In order to filter the strain fields of individual grains, however, the GM needs to correspond to the DIC reference state. The pre-pattern mask is transferred to the point-O micro-DIC field [Fig. 1(a)] by an affine transformation, after which the results are re-verified using microstructural features (e.g., triple points). Over Fig. 1(a), the GB network of the point-O GM (derived with an edge operator) is shown in red.

In this study, multiple load points are considered as DIC reference points (RPs) over the unload (a robustness measure, "Internal Measures of Robustness" section). RP-O GM is not valid for other RPs due to deformation, and the GM that is specific to each RP is generated by deformation mapping. This uses micro-DIC displacement results calculated among the target RP and point O. Such mapping operations have been described in detail in Özdür et al. [22] applied to images; here, they are applied to GMs. Note, GM mapping simply replaces the labor of repetitive GB drawing at each RP; each GM is anyhow verified against microstructural features (see "Results" section).

DIC Averaging

The fact that averaging of the DIC fields improves the precision of the average (while sacrificing resolution) is known and commonly utilized (e.g., deriving the stress-strain curve of a tensile test from DIC measurement). One way to explain this effect is noting that the DIC strain uncertainty goes by the DIC displacement uncertainty divided by the data spacing and, upon averaging, the *effective data spacing* is expanded to the chord length of the averaging domain[1]. Thus, averaging roughly reduces DIC uncertainty by a factor $1/n$ where n is the number of data points averaged *over a single dimension*. Hence, for the characteristic grain sizes (~ 25 μm) and data spacing (1 μm) here, an accuracy gain, $n \sim 25$, might be postulated for *grain-averaged* strains. Given the aforementioned local DIC uncertainty, this crudely implies a grain-averaged strain uncertainty about 20 $\mu\varepsilon$.

These postulates, however, are based on normal distributions, whereas large-scale DIC data is bound to contain outliers. Consequently, all operations (average, standard deviation, etc.) over strain fields are performed with robust estimators, by a recursive removal of points outside three standard deviations (sigma clipping [40]). The number of removed points typically remain very limited, however ($< 0.2\%$).

[1] For a quick sketch of this notion, consider a one-dimensional displacement array u_i, i = 1,...,n+1 and a simplistic determination of strain with $\varepsilon_i = (u_{i+1} - u_i)/\Delta$, where Δ is the data spacing. The average strain over N data points can easily be simplified to $\overline{\varepsilon} = (u_{n+1} - u_1)/(n\Delta)$, noticing the successive cancellations. If δu represents the displacement uncertainty, the uncertainties in local and averaged strains are $\delta\varepsilon_i = 2\delta u/\Delta$ and $\delta\overline{\varepsilon} = 2\delta u/(n\Delta)$, respectively, where $n\Delta$ is the chord length of the averaging domain.

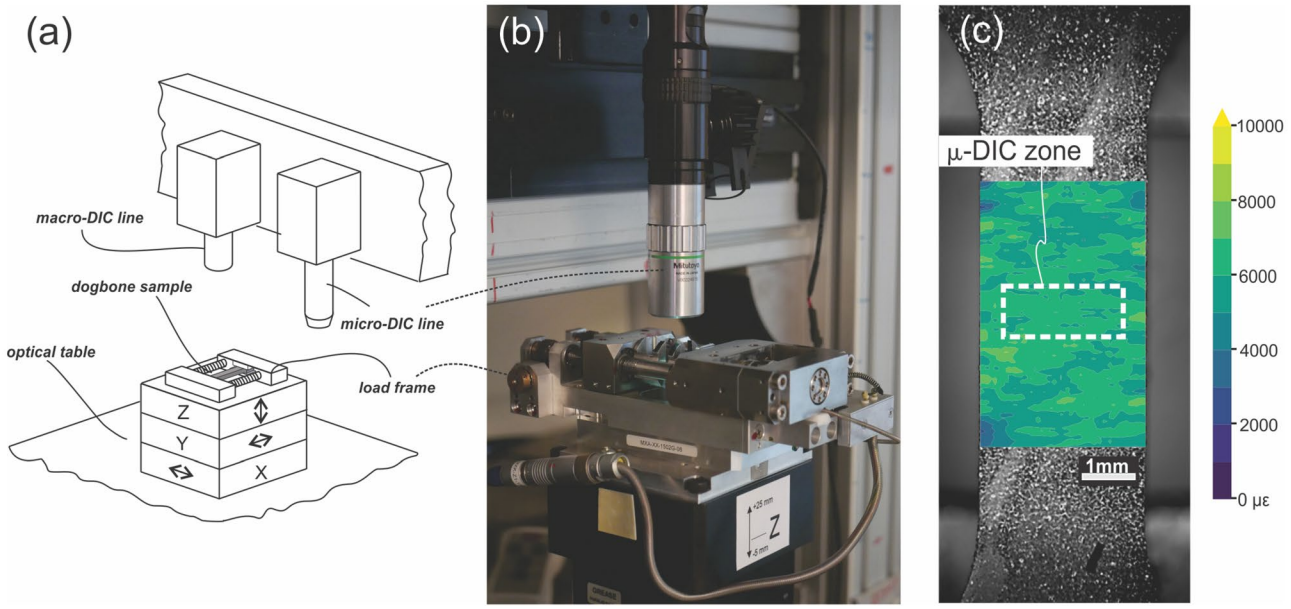

Fig. 2 (**a**) Sketch of the experimental setup, (**b**) close-up photo of micro-DIC optics, load frame and *Z*-stage, (**c**) macro-DIC image overlaid with axial macro-DIC strain field at point T (see Fig. 4). The μ-DIC zone indicated with a box

Grain averages are denoted by overbars, e.g., $\overline{\varepsilon}_{22}$ stands for the grain-averaged axial strain. The designation for full-field average (which is also the average over all grains) is further enveloped by angle brackets, e.g., $\langle\overline{\varepsilon}_{22}\rangle$.

With the applied stress, σ_{app}, defined as load divided by cross-sectional area, general conformance to the uniaxial stress state over a *representative* micro-DIC domain dictates:

$$\langle\overline{\sigma}_{22}\rangle = \sigma_{app}\ ,\ \langle\overline{\sigma}_{11}\rangle = 0\ ,\ \langle\overline{\sigma}_{12}\rangle = 0\,. \tag{1}$$

Estimation of the Average Grain Stress via a Partial Unload

First, consider a one-dimensional (1-D) analogy/verification over Fig. 4. T, U designate the top and fully-unloaded points, respectively. U′ is the (hypothesized) point of full *elastic* unload. Defining U′ is hardly necessary in this analogy, but will be conceptually important in the actual tensorial case that is brought up next. Suppose elastic compliance $S = d\varepsilon/d\sigma_{app}$ is measured by fitting the data points over an unload, only considering those (shown with blue-bold markers) that largely precede significant reverse plasticity. With trivial trigonometry, the estimate for elastic strain release upon unload is then $\varepsilon_{el} = S(\sigma^T_{app} - \sigma^{U'}_{app}) = S\,\sigma^T_{app}$ with $\sigma^{U'}_{app} = 0$. Also considering $\sigma^T_{app} = E\,\varepsilon_{el}$, where E is the tabulated Young's modulus, one gets

$$\sigma^T_{app} = E(S\,\sigma^T_{app})\,. \tag{2}$$

Here, to serve the analogy, the quantities in the parentheses are experimentally measured, whereas E is gathered from literature. Clearly, a trivial equality $\sigma^T_{app} = \sigma^T_{app}$ ensues with an expected $E = 1/S$ for this 1-D case.

To construct the required tensorial case for stress estimation of a grain with orientation $\mathbf{g}$, single crystal elastic constants (Table 1) are gathered from literature (instead of E in the 1-D analogy). σ_{app} now is reduced to a load parameter, proportional to the measured $\overline{\varepsilon}_{\alpha\beta}$, $\alpha,\beta = 1,2$ over the partial unload. For each $(\overline{\varepsilon}_{\alpha\beta}, \sigma_{app})$ data set in this range, the stress slope

$$\tilde{S}_{\alpha\beta} = \frac{\partial\overline{\varepsilon}_{\alpha\beta}}{\partial\sigma_{app}}\ ,\ \alpha,\beta = 1,2 \tag{3}$$

is once more found by linear regression. The grain-averaged stress estimate in analogy to equation (2) (with measured quantities again in parentheses), is then given by

$$\overline{\sigma}^{TU'}_{\alpha\beta} = \mathbf{C}^{\mathbf{g}}(\tilde{S}_{11}\sigma^T_{app}, \tilde{S}_{22}\sigma^T_{app}, \tilde{S}_{12}\sigma^T_{app}) \tag{4}$$

$$\overline{\sigma}^{TU'}_{\alpha\beta} = \overline{\sigma}^{T}_{\alpha\beta} - \overline{\sigma}^{U'}_{\alpha\beta} \tag{5}$$

$$\tilde{S}_{\alpha\beta}\sigma^T_{app} = \overline{\varepsilon}^{T}_{\alpha\beta,el} - \overline{\varepsilon}^{U'}_{\alpha\beta,el}\ ,\ \ \alpha,\beta = 1,2 \tag{6}$$

The complication that the reference state U′ is retained in equations (4)–(6) is physically due to the fact that when the aggregate is elastically unloaded (with the aggregate-average assuming $\sigma^{U'}_{app} = 0$ at U′), individual grains do not have to

Table 1 Pure Ni elastic constants in stiffness and compliance [41] (first row); anisotropy ratio (AR), extremal values of isostress stiffness and compliance (second row); utilized DAMASK [42] phenopower law constants for spectral analysis (third row)

c_{11} (in GPa)	c_{12}	c_{44}	s_{11} (in TPa^{-1})	s_{12}	s_{44}
246.5	147.3	124.7	7.34	−2.74	8.02
AR E_{100} ; E_{111} (GPa)			E^{-1}_{100} ; E^{-1}_{111} (TPa^{-1})		
2.51 136.2; 303.6			7.34; 3.29		
$\dot{\gamma}_0(s^{-1})$	ξ_0	ξ_∞(MPa)	h_0(GPa)	α	n
10^{-3}	29.1	240	0.97	2.25	83.3

realize a zero stress state (but just a zero sum). "On the Stress Formalism" section will further discuss $\overline{\sigma}^{U'}_{\alpha\beta}$ as a type-II residual stress field. Currently, note $\overline{\sigma}^{T}_{\alpha\beta} \gg \overline{\sigma}^{U'}_{\alpha\beta}$ is typical, in which case, the point-T stress is approximated well by equation (4), i.e., $\overline{\sigma}^{T}_{\alpha\beta} \simeq \overline{\sigma}^{TU'}_{\alpha\beta}$. As for aggregate averages, this obviously becomes an equality

$$\langle \overline{\sigma}^{TU'}_{\alpha\beta} \rangle = \langle \overline{\sigma}^{T}_{\alpha\beta} \rangle - \cancelto{0}{\langle \overline{\sigma}^{U'}_{\alpha\beta} \rangle} \tag{7}$$

since $\langle \overline{\sigma}^{U'}_{\alpha\beta} \rangle = 0$ (equation (1), with $\sigma^{U'}_{app} = 0$).

The linear operator $\mathbf{C}^{\mathbf{g}}$ in equation (4) stands for the elastic constitutive relationship for orientation $\mathbf{g}$ that is embedded the traction-free boundary conditions of this surface measurement (details in Appendix). The role of linear regression (in defining $\tilde{S}_{\alpha\beta}$ in equation (3) or S in Fig. 3) is to enhance the accuracy of elastic strain estimate (equation (6)) by using multiple data points.

Writing out the terms of equation (3) by incorporating equation (1),

$$\tilde{S}_{22} = \frac{\partial \overline{\varepsilon}_{22}}{\partial \langle \overline{\sigma}_{22} \rangle}; \quad \tilde{S}_{11} = \frac{\partial \overline{\varepsilon}_{11}}{\partial \langle \overline{\sigma}_{22} \rangle}, \tilde{S}_{12} = \frac{\partial \overline{\varepsilon}_{12}}{\partial \langle \overline{\sigma}_{22} \rangle} \tag{8}$$

explains the switch to a neutral term, stress slope, for $\tilde{S}_{\alpha\beta}$. Specifically, numerator-denominator components do not agree for either $\tilde{S}_{11}$ or $\tilde{S}_{12}$, making these merely slopes with respect to the loading parameter, σ_{app}. Only $\tilde{S}_{22}$ can be considered an *apparent* compliance with matching components.

Crystal Plasticity Calculations

Spectral analysis with DAMASK is used for its high efficiency. Columnar grain domains are produced directly from the actual EBSD maps with Dream3D [43]. The voxel size of the analyses nominally obey the 3 μm spacing of the EBSD scans. The material constants of its standard power-law viscoplastic model [42] are tuned to fit the stress-strain curve of the current experiment (Fig. 4) within 2% (see Table 1). For comparison with the experiment data over the unload, the DAMASK analysis is also appended an unload step after plastic straining. Domain images, basic formulation and representative results for the DAMASK analysis are provided in the Supplementary Material.

For a general measure of crystallite stiffness, we also consider *single-crystal* effective modulus (E_{hkl}) and compliance (E^{-1}_{hkl})

$$E^{-1}_{hkl} = s_{11} + \frac{(2s_{12} - 2s_{11} + s_{44})(h^2k^2 + k^2l^2 + h^2l^2)}{(h^2 + k^2 + l^2)^2} \tag{9}$$

corresponding to a tensile test along direction [*hkl*] [41]. For a polycrystal, these stand for the axial stiffness and compliance under the limiting isostress (Sachs [44]) assumption. Note the extremal values (E_{111} and E_{100}) in Table 1.

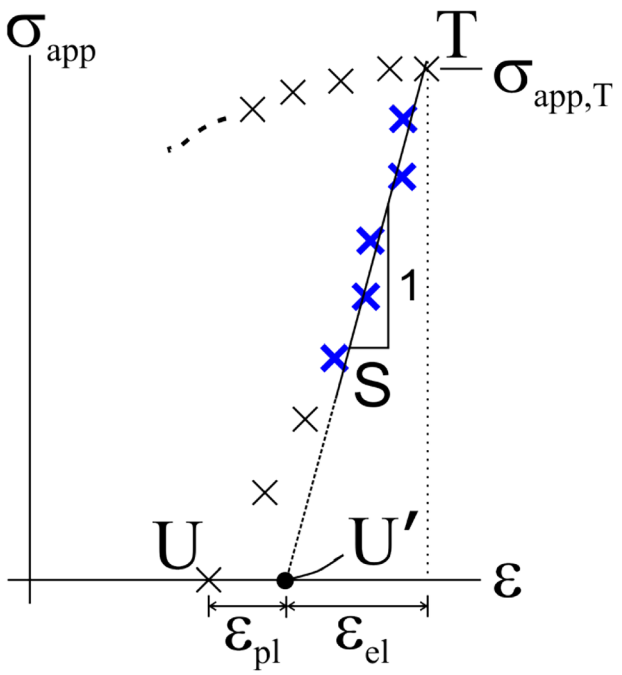

Fig. 3 One dimensional analogy of the stress estimation idea by fitting compliance S over the initial segment of the unload. ε_{el}, ε_{pl} refer to elastic and (reverse-)plastic strains

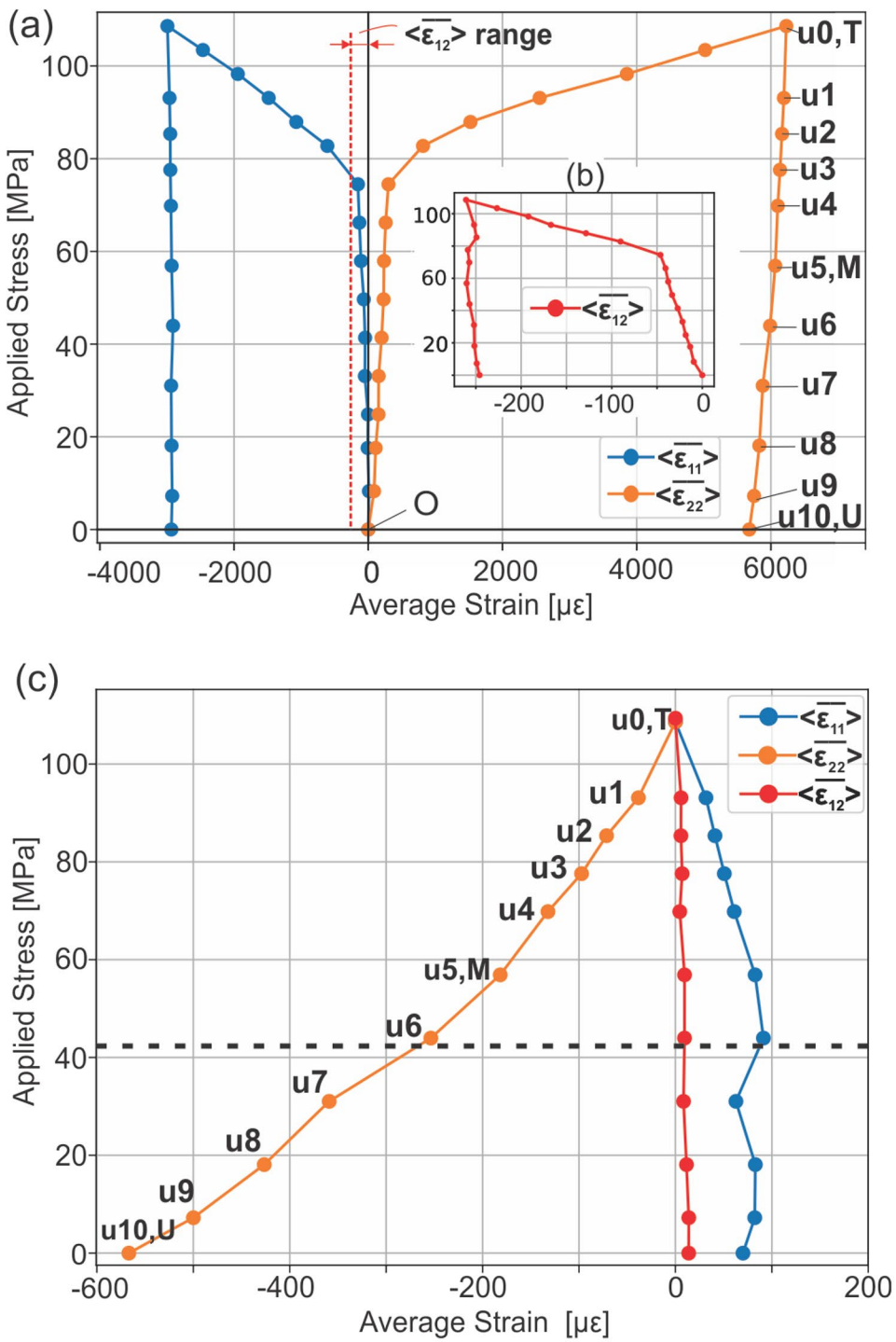

Fig. 4 Applied stress plotted versus aggregate-average (**a**) axial, $\langle\bar{\varepsilon}_{22}\rangle$, and transverse strain $\langle\bar{\varepsilon}_{11}\rangle$, (**b**) shear strain $\langle\bar{\varepsilon}_{12}\rangle$ (DIC calculation with reference point O); (**c**) applied stress versus aggregate-average strains only over the unload (DIC calculation with reference point T)

Internal Measures of Robustness

Two measures are incorporated in the DIC analysis to evaluate the robustness of the results. The first is using multiple reference load points (RPs), which actually implies a full repetition of the DIC analysis at each RP. While not typically undertaken, this check is available for any *in situ* DIC study. If the results are robust/objective, when the RP is altered, the computed trends should remain equivalent aside from a trivial shift in strains.

Three RPs are picked here: top (T), full-unload (U), (Figs. 3 and 4) and unload midpoint (M) (Fig. 4). Note, when the RP is changed, virtually all image pairs used in DIC calculations are changed, making it an independent test in this regard. Further, the aforementioned strain shift associated with altering the RP is not even a factor when computing the *slopes* in equation (3).

The second measure of robustness employs binary morphology over the grain mask (GM) that defines the region of the grain over the strain fields. Accordingly, if the GM is stripped one data layer (only a 1 μm band at the outside boundary) and the calculations repeated, the results should only show a contained physical change. The reason erosion is considered as a robustness measure is related to the fact that, averaging will tend to annul the effect of outliers inside the averaging region, but is more vulnerable against those on the boundary (observe, e.g., over footnote 1 in "DIC Averaging" section, by making u_{n+1} an outlier). So, if we gently alter the boundary by stripping a small distance, huge variations will point to surface outliers and an unreliable estimate, while a contained variation will indicate robust results.

In application, the reported grain averages already correspond to one-layer-stripped ($n = 1$) GMs to avoid the outermost data ring that has significant subset overlap with the neighboring grains. We will consider analyses after stripping $n = 2, 3, 4$ layers as well (the final 4 μm erosion is still small compared to the large grains) and expect small variations among these.

The discrepancy measure considered for each $\tilde{S}_{\alpha\beta}$, combines independent calculations with RP = T, M, U, and erosions $n = 1, 2, 3, 4$, yielding a set of 12 results. The standard deviation of each set is called $\delta\tilde{S}_{\alpha\beta}$ and a scalar discrepancy is defined as

$$D = \sqrt{\frac{1}{3}(\delta\tilde{S}_{11}^2 + \delta\tilde{S}_{22}^2 + \delta\tilde{S}_{12}^2)} \tag{10}$$

to rank the reliability of the grains.

Results

Aggregate Average

Figure 4(a) shows the type-I results of the DIC analysis (conducted with RP-O), averaged over the entire micro-DIC domain of Fig. 1(a) that comprises approximately 5000 grains. $\langle\overline{\varepsilon}_{22}\rangle$ and $\langle\overline{\varepsilon}_{11}\rangle$ are the axial and transverse strains, respectively. Figure 4(a) shows the entire load history, with markers indicating the micro-DIC scan points. The unload we will focus on, contains 11 micro-DIC points u0,...,u10. The aggregate-average $\langle\overline{\varepsilon}_{12}\rangle$ is extremely limited [range in Fig. 4(a)], with magnitudes around 1/30th the axial strains. Normally, this would only be noted as a perfectly acceptable approximation to the targeted uniaxial stress state, however, we further zoom into the very limited strain interval of $\langle\overline{\varepsilon}_{12}\rangle$ in the inset Fig. 4(b) to present that the $\mu\varepsilon$ trends of $\langle\overline{\varepsilon}_{12}\rangle$ (over initial linear ramp, plasticity, and unload) are also resolved, demonstrating the amplified sensitivity of the DIC measurement upon averaging. Note the stylistic choice of using $\mu\varepsilon$ (microstrain) units all through the manuscript over Fig. 4(a), (b). This promotes the fair evaluation of the varying strain ranges in the plots, noticing magnitudes [e.g., Fig. 4(b)] that are outside the typical DIC accuracy.

Figure 4(c) (another plot in this category) zooms into the unload for full-field averages. The DIC here is conducted with respect to point T, yielding a zero strain value at T for a direct presentation of strains that are realized over the unload. There is a linear trend in $\langle\overline{\varepsilon}_{22}\rangle$ and $\langle\overline{\varepsilon}_{11}\rangle$ in the initial segment of the unload that falters after u6, signified by a dashed line in Fig. 4(c). The partial unload range over which the behavior of the polycrystal is regarded to be virtually elastic is accordingly determined, and u1,...,u6 are taken as the unload points over which the slopes are henceforth determined. The slopes of the aggregate data in Fig. 4(c) for $\partial\langle\overline{\sigma}_{22}\rangle/\partial\langle\overline{\varepsilon}_{22}\rangle$ and $\partial\langle\overline{\sigma}_{22}\rangle/\partial\langle\overline{\varepsilon}_{11}\rangle$ (again, recall equation (1)) over the range u1-u6 are 240 and -710 GPa, respectively. Both fits have a r-squared value above 0.98. The division of these slopes yield a Poisson's ratio, $-\partial\langle\overline{\varepsilon}_{11}\rangle/\partial\langle\overline{\varepsilon}_{22}\rangle$, of 0.338. The domain-averaged DAMASK results over the unload are largely consistent, with 232 GPa for axial stiffness and 0.3 for Poisson's ratio. With $\langle\overline{\varepsilon}_{12}\rangle$ remaining near null as well; these type-I results describe a perfectly sensible elastic unload (of a uniaxial stress state) in the prescribed range, u1-u6.

Incidentally, the elastic Poisson's ratio can be put in perspective of 0.5 that is virtually equal to the division of point-T *total* transverse strain ($-3215\ \mu\varepsilon$) to its *total* axial strain ($6450\ \mu\varepsilon$) on Fig. 4(a). This is the ideal value of the strain ratio after isochoric *plastic* strains dominate in a (transversely) isotropic material—sensible given the transverse isotropy of the extruded sample [26].

For plastic strains, which are outside the general scope here, DIC can yield type-III results with the full 1 μm spatial resolution. Consider the *total*-ε_{22} fields [Fig. 5(b)] at point T (*total*: DIC with respect to RP-O) in a representative material neighborhood [Fig. 5(a)]. These fields portray the typical physics of polycrystal plasticity with loose $\pm 45°$ banded formations [2], by clearly rising above the measurement uncertainty.

In contrast, Fig. 5(c) presents ε_{22} fields over a limited unload, with DIC among load u2 and RP-T, where the minute physical deformation signal [average about 70 $\mu\varepsilon$ from T to u2, Fig. 4(c)] is clearly buried under the noise floor. Hence, no type-III results with full spatial resolution is available for these elastic strain fields. The next section delves into the premise of the study: locally average the fields over respective grains to evaluate if the resulting noise cancellation ("DIC Averaging" section) can yield type-II physical measurements of elastic strains.

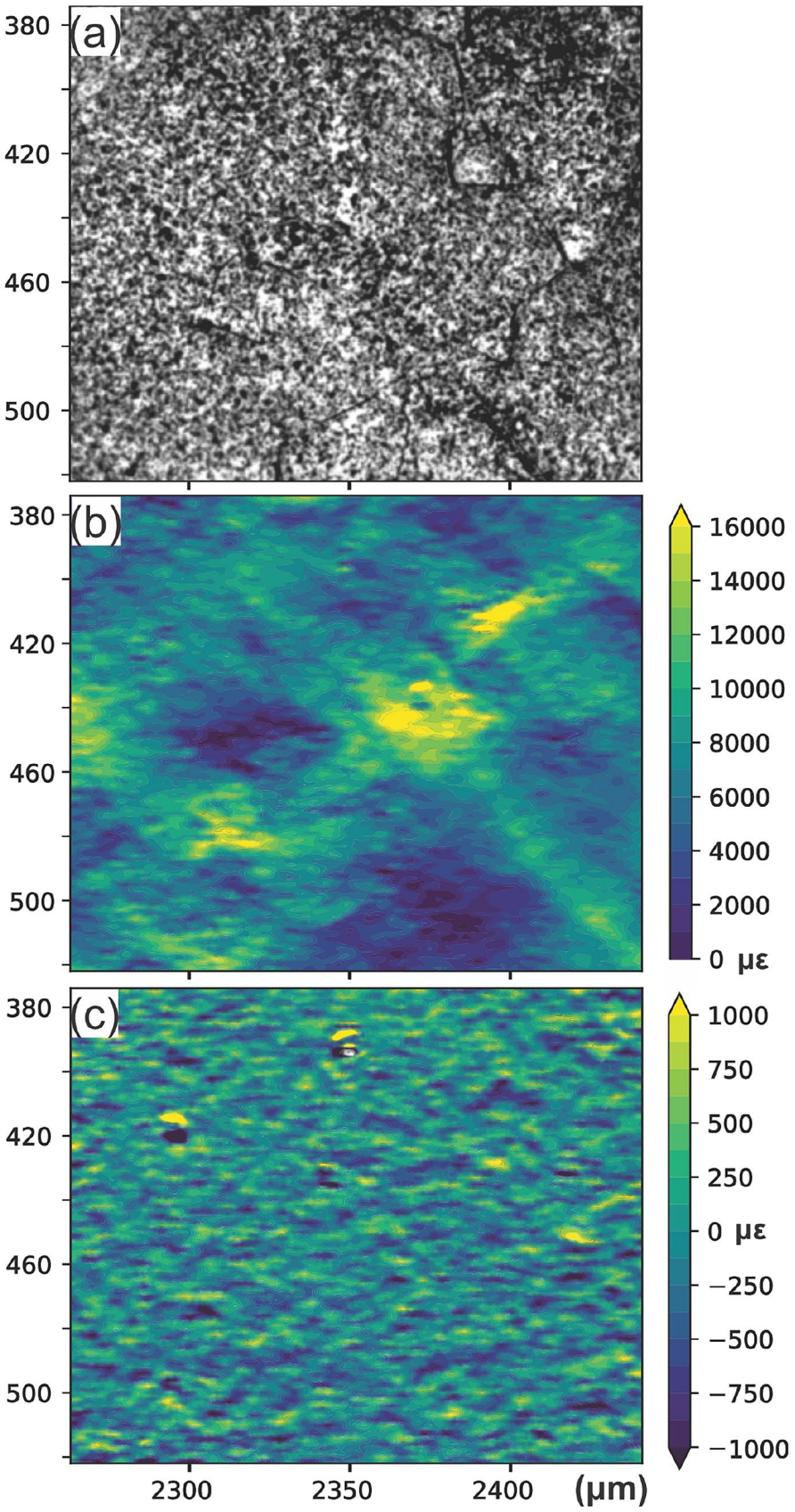

Fig. 5 (**a**) An $150 \times 180\ \mu m^2$ grain neighborhood over which DIC results are shown with contour plots: (**b**) total axial strains, ε_{22}, at point T, (**c**) incremental axial strain field upon a nominal 15 MPa unload (second unload point u2 calculated with respect to top point T). See Fig. 4 for load point definitions

Selected Individual Grain Evaluations

Figure 6 combines all salient features of the proposed grain-resolved assessment, specialized to a well-behaved grain called grain A [45]. The first row pertains to morphology. Recall stitched image fields at different RPs T, M and U are independent as well as their GMs ("Grain Mask" section). Figure 6(a) is the bare image crop (about grain A) from RP-T image fields, whereas Fig. 6(b) is the GM generated for RP-T overlaid on this crop. Figure 6(c) and (d) are the equivalent plots from image fields and GMs of RP-M and RP-U, respectively. Through the visible triple point on the left side (marked with an arrow) as well as other prominent features/speckles, note that each GM correctly identifies the grain(s) despite the natural variations in $x_1 - x_2$ axes among the field coordinates of the three load points [inspect the axes in Fig. 6(b–d)]. This also means that the field correspondences would not be correct without adequate GM-mapping. The second row, Fig. 6(e–h), presents the statistics of the data cloud inside the grain (3228 data points) for independent DIC calculations with respect to RP-T, RP-M and RP-U. Specifically, the u2-result in Fig. 6(e) corresponds to the u2-image analyzed with respect to load-T image, whereas the same point in Fig. 6(h) corresponds to u2-image analyzed with respect to load-U image. The zero-strain in each case naturally shifts to the corresponding RP: the zero-axis passes through T, M and U in Fig. 6(e), (g), and (h), respectively.

The blue and pink shades in Fig. 6(e–h) correspond to the one and two standard deviation ($\sigma, 2\sigma$) envelopes of the grain-A data cloud for each load point. For RP-T, Fig. 6(e) envelopes can be paired with actual histograms, provided for selected loads in Fig. 6(i). The data percentage inside (σ and 2σ) envelopes at each DIC point is calculated (for RP-T, ε_{22}, median 69.8 and 95.4%, respectively), and this near conformance to the Gaussian-distribution bounds (68.3 and 95.5%), applies to all RPs and strain components ε_{22}, ε_{11}, ε_{12} (For brevity, Fig. 6(e–i) consider ε_{22} only). The grain average is shown with markers at the center of each cloud in Fig. 6(e–h). The main point—highlighted by adding the ε_{22} values for a single data point CM (chosen at the grain centroid [46]), and a data-range zoom in Fig. 10(f)—is clear: although individual data points are severely scattered (noise much larger than signal), their average demonstrates the physical trend of the unload similar to the full-field average, Fig. 4(c).

The grain averages for all components are put together in Fig. 6(j), with sensible behavior observed in each. The linear fits (performed in the fitting interval u1-u6, highlighted with yellow) are added to the figure and labeled by their slopes, $\tilde{S}_{\alpha\beta}$.

Figure 6(j) shows RP-T calculations, but that is hardly important for grain A with exceptionally low RP-discrepancy. Valid for all components, this is presented for ε_{22} in Fig. 6(k); the data points are virtually coincident when RP-M and RP-U grain-averages [from Figs. (g), and (h)] are appropriately shifted[2] onto RP-T results.

Figure 6(l) presents the process of producing consecutively larger regions about the grain core, though by a backwards process of layer-by-layer stripping (layers counted by n) from the full grain mask. Each region is called R with corresponding area, A. (With the virtual 1 μm data-spacing, A in μm^2 also corresponds to the number of data points in R.)

The entire process of region-averaging and linear fitting is carried out for all R, and the results are plotted against $\sqrt{A}$ (in μm), generating Fig. 6(n–p) for the slopes $\tilde{S}_{\alpha\beta}$ and Fig. 6(m) for the correlation coefficient. The robustness criteria ("Internal Measures of Robustness" section) of near-equivalence-of-$\tilde{S}_{\alpha\beta}$ over $n = 1, .., 4$ concerns the last four data points, highlighted by a yellow band. To interpret $A \to 1$, the left limit of the graphs that corresponds to a single data point at the centroid, one can revisit CM-data in Fig. 6(e), noting that a fit to this level of noise is not meaningful. Indeed, r-values in Fig. 6(m) only reach decent values after a certain size of the averaging domains. Below this, as the figurative gray-shading indicates, the $\tilde{S}_{\alpha\beta}$ values are not to be considered. The use of r (instead of its square) in Fig. 6(m) underlines the opposite-sense correlations of $\overline{\varepsilon}_{22}$ and $\overline{\varepsilon}_{11}$ with σ_{app}. ($\overline{\varepsilon}_{12} \sim 0$ is hardly correlated with σ_{app}, making its r-values non-informative and small—in general, $r \to 0$ for zero-slope data).

Leaving intragranular variations in $\tilde{S}_{\alpha\beta}$ to discussion, observe that RP-T, RP-M and RP-U calculations yield a strong agreement for $\tilde{S}_{\alpha\beta}$ in Fig. 6(n–p) in the robustness-criterion range (yellow band). To quantify, the standard deviations, $\delta\tilde{S}_{\alpha\beta}$ of 12 data points in this band are provided in Table 2 (column 6). Discrepancy (equation (10)), $D = 0.06$ TPa^{-1} is two orders below the $\tilde{S}_{22}$ for grain A. The means of the 12 data points are reported as $\tilde{S}_{\alpha\beta}$ in Table 2 (column 5), and used in the grain-averaged stress calculation of equation (4). The resulting type-II estimates for point-T stress state are provided in the last column.

The orientation matrix of grain A (Appendix) is provided in Table 2, where the emphasized second row corresponds to the crystal direction aligned with load (i.e., hkl in E_{hkl}). Judging by the basic stiffness (compliance) measure of E_{hkl} (E^{-1}_{hkl}) in Table 2, grain A is rather compliant. Notice $\tilde{S}_{22} = 6.01$ TPa^{-1} admits a comparison with $E^{-1}_{hkl} = 5.8$TPa^{-1}.

Three more grains (B, C, D) that cover a range of elastic stiffness (see E_{hkl} in Table 2) are presented in Fig. 7 with condensed results. In Fig. 7, each row corresponds to a grain.

[2] The strain shift value for RP-M (RP-U) is determined as the distance between the center of mass of the linear fit for the RP-M (RP-U) data and the RP-T data.

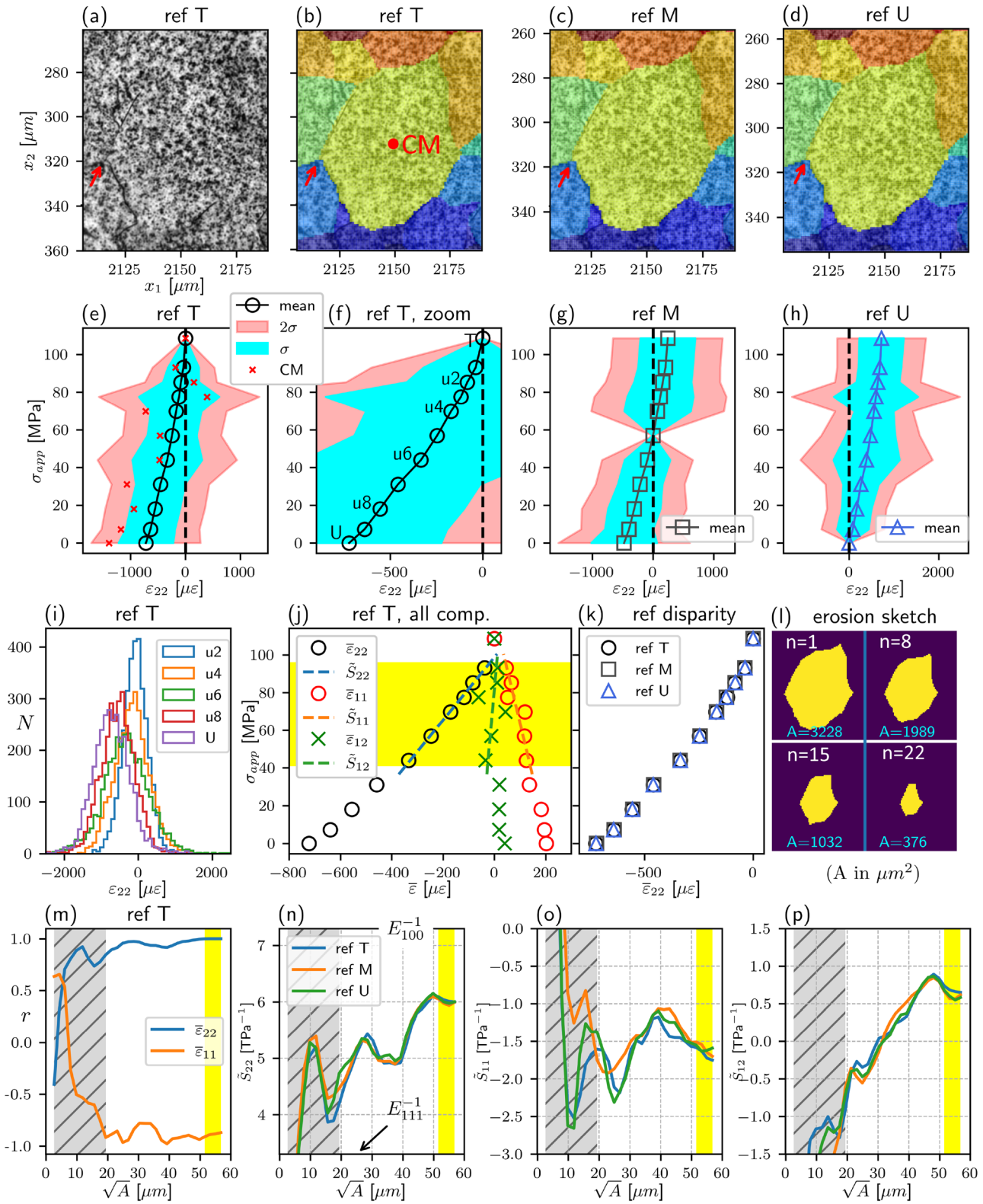

Fig. 6 (**a**) DIC image of a neighborhood about target grain A recorded at reference point (RP) T, (**b**), (**c**), (**d**) RP-specific grain masks in arbitrary coloring (grain A in yellow) overlaid with a degree of transparency on the images recorded at each RP (T, M and, U). Plotted against applied stress (σ_{app}), ε_{22} data clouds in grain A within 1 and 2 standard deviations ($\sigma, 2\sigma$) about the mean $\bar{\varepsilon}_{22}$ at RP (**e**), (**f**) T, (**g**) M, and (**h**) U. ε_{22} data point at grain centroid (CM) is appended in (**e**). (**i**) Grain-A ε_{22} histograms at selected load points, **j** all grain-averaged components, $\bar{\varepsilon}_{22}$, $\bar{\varepsilon}_{11}$, $\bar{\varepsilon}_{12}$ from RP-T calculations (slope evaluation range highlighted; fits labeled by their slopes $\tilde{S}_{\alpha\beta}$). (**k**) Aligned $\bar{\varepsilon}_{22}$ results at all RPs, (**l**) different-sized regions R (each with area A), considered about the core of grain A obtained via erosion, (**m**) correlation coefficient, r, of fits [as in (**j**)] but for $\bar{\varepsilon}_{11}(R)$ and $\bar{\varepsilon}_{22}(R)$, (**n**) $\tilde{S}_{22}(R)$, (**o**) $\tilde{S}_{11}(R)$, (**p**) $\tilde{S}_{12}(R)$ plotted with respect to $\sqrt{A}$ of grain region R

Table 2 Information and results table for selected grains A, B, C, D

G	**Orientation** [g_{ij}]	**Area**(μm^2)	E_{hkl} (GPa) E^{-1}_{hkl} (TPa^{-1})	$\tilde{S}_{22}, \tilde{S}_{11}, \tilde{S}_{12}$ (TPa^{-1})	$\delta\tilde{S}_{22}, \delta\tilde{S}_{11}, \delta\tilde{S}_{12}$ D (r.m.s.) (TPa^{-1})	$-\frac{\tilde{S}_{11}}{\tilde{S}_{22}}$	$\frac{\tilde{S}_{12}}{\tilde{S}_{22}}$	$\overline{\sigma}^{TU'}_{22}, \overline{\sigma}^{TU'}_{11}, \overline{\sigma}^{TU'}_{12}$ (MPa)
A	0.95 −0.07 0.30 **−0.05 0.92 0.38** −0.30 −0.38 0.88	3433	172 (5.80)	6.01, −1.62, 0.63 (*4.95, −1.92, −0.19*)	0.04, 0.07, 0.06 (0.06)	0.27 (*0.39*)	0.10 (*−0.04*)	125, 25, 16 (*99, 7, −2*)
B	0.75 0.24 0.60 **−0.56 0.73 0.39** −0.35 −0.64 0.68	1654	268 (3.62)	4.14, −1.37, −0.08 (*4.55, −1.03, −0.32*)	0.15, 0.17, 0.09 (0.14)	0.33 (*0.25*)	−0.02 (*−0.08*)	119, −4, −1 (*116, −2, 9*)
C	0.78 0.62 −0.11 **−0.57 0.62 −0.54** −0.27 −0.48 0.84	1264	301 (3.32)	4.93, −0.68, 0.77 (*4.20, −0.62, −0.51*)	0.22, 0.5, 0.26 (0.35)	0.14 (*0.14*)	0.16 (*−0.12*)	162, 8, 3 (*122, 6, 4*)
D	0.81 0.13 −0.57 **−0.38 0.86 −0.34** 0.44 −0.50 0.75	932	209 (4.78)	5.20, −0.82, −0.06 (*4.57, −1.29, −0.75*)	0.53, 0.55, 0.20 (0.46)	0.16 (*0.28*)	−0.01 (*−0.16*)	131, 32, −4 (*122, 5, 2*)

Italicized results in parentheses refer to the spectral model

The first and second columns are analogous to Fig. 6(b) and (j), respectively. The third column is a combination of Fig. 6(n–p) with a focused range about the (yellow) robustness-criterion ($n = 1, ..., 4$) band.

Inspecting Table 2 for detailed results, one notes the more limited $\tilde{S}_{22}$ for these stiffer grains. In this regard, it is important to compare $\overline{\varepsilon}_{22}$ in Figs. 6(j), 7(b), (e), and (h) where the strain-axis ranges are kept identical, while also keeping the field average [Fig. 4(c)] in sight. There is noticeable variation in $-\tilde{S}_{11}/\tilde{S}_{22}$, that can be perceived as a grain-effective Poisson's ratio. Large variations in this quantity are supported by the spectral simulation (the italicized results in Table 2 in parentheses). The loading direction ($\tilde{S}_{22}$, $\overline{\sigma}^{TU'}_{22}$) predictions are, however, more regulated compared to the experiment. $\tilde{S}_{12}/\tilde{S}_{22}$ column shows small shear magnitudes compared to axial strains.

The experimental stress results in Table 2 are largely sane in terms of proximity to the effective uniaxial stress state, with comparatively low $\overline{\sigma}^{TU'}_{11}$ and $\overline{\sigma}^{TU'}_{12}$, and $\overline{\sigma}^{TU'}_{22}$ values that are comparable to the applied stress at point T, $\sigma^{T}_{app} = 108.1$ MPa.

Naturally, an accompanying model can also output absolute stress values. Thus, $\overline{\sigma}^{T}_{\alpha\beta}$ and $\overline{\sigma}^{U'}_{\alpha\beta}$ are available separately from the spectral simulation, as well as their difference (equation (5)) tabulated in Table 2. In any polycrystal model, $\overline{\sigma}^{U'}_{\alpha\beta}$ can be calculated via equations (5) and (6), after a limited elastic unload from point T (note $\overline{\sigma}^{T}_{\alpha\beta}$ already computed) to yield $\tilde{S}_{\alpha\beta}$. The DAMASK standard model did not possess any kinematic hardening and produced a full elastic unload anyway. Hence, $\overline{\sigma}^{U'}_{\alpha\beta}$ could also be directly gathered as unload point stresses. $\overline{\sigma}^{U'}_{\alpha\beta}$ in the model are limited compared to $\overline{\sigma}^{T}_{\alpha\beta}$, in agreement with the expectation in "Estimation of the Average Grain Stress via a Partial Unload" section. To quantify, the mean value of absolute $|\overline{\sigma}^{U'}_{\alpha\beta}|$ components is calculated for each grain, yielding less than 5.4 MPa in all four grains.

Statistics

While the difficult premise that entails detecting minute strain magnitudes has been demonstrated over selected grains, the stern quality of the necessary measurement is not realized on a wide scale (discussion in "Proof of Concept over Sporadic grains" section). Figure 8 presents the histogram of the postulated discrepancy, D for grains in the aggregate. D is predominantly decided by the consistency of slopes when DIC analyses are repeated with respect to different reference loads. For the delicate quantity of $\tilde{S}_{\alpha\beta}$ over an unload, few grains did well with this objectivity measure, and D magnitudes are mostly comparable to (or bigger than) actual apparent compliances.

To select *sane* grains, first, an arbitrary D limit (=0.6 TPa^{-1}) is set about an order below the apparent compliance. (Note, if, e.g., D is demanded to be an order lower, only the most stellar grain, grain A, would meet the limit.) Applying another filter on data linearity,[3] 43 grains are selected. Figures 9 and 10 plot their stress-slopes and type-II stresses against the spectral analysis predictions. In these square plots, a diagonal near-equality band (blue) is added to aid the eye. This does not, however, imply that spectral analysis results are simply *true*, and the experimental results are judged against them. As we will discuss further ("Complementary Modeling" section), spectral analysis only yields a sanity comparison, one that appears to be more suited than simple isostress predictions. Note, experimental $\tilde{S}_{22}$ paired with spectral-analysis $\tilde{S}_{22}$ in Fig. 9(a) is less dispersed than

[3] This is a combined limit $r(\varepsilon_{22})r(\varepsilon_{11}) < -0.4$ to allow some decent grains, e.g., grain C, with stellar $r(\varepsilon_{22})$ but poor $r(\varepsilon_{11})$. Over the 43 selected grains, mean $r(\varepsilon_{22}) = 0.88$ whereas mean $r(\varepsilon_{11}) = -0.73$ decidedly worse. This likely pertains to the more limited $r(\varepsilon_{11})$ signal.

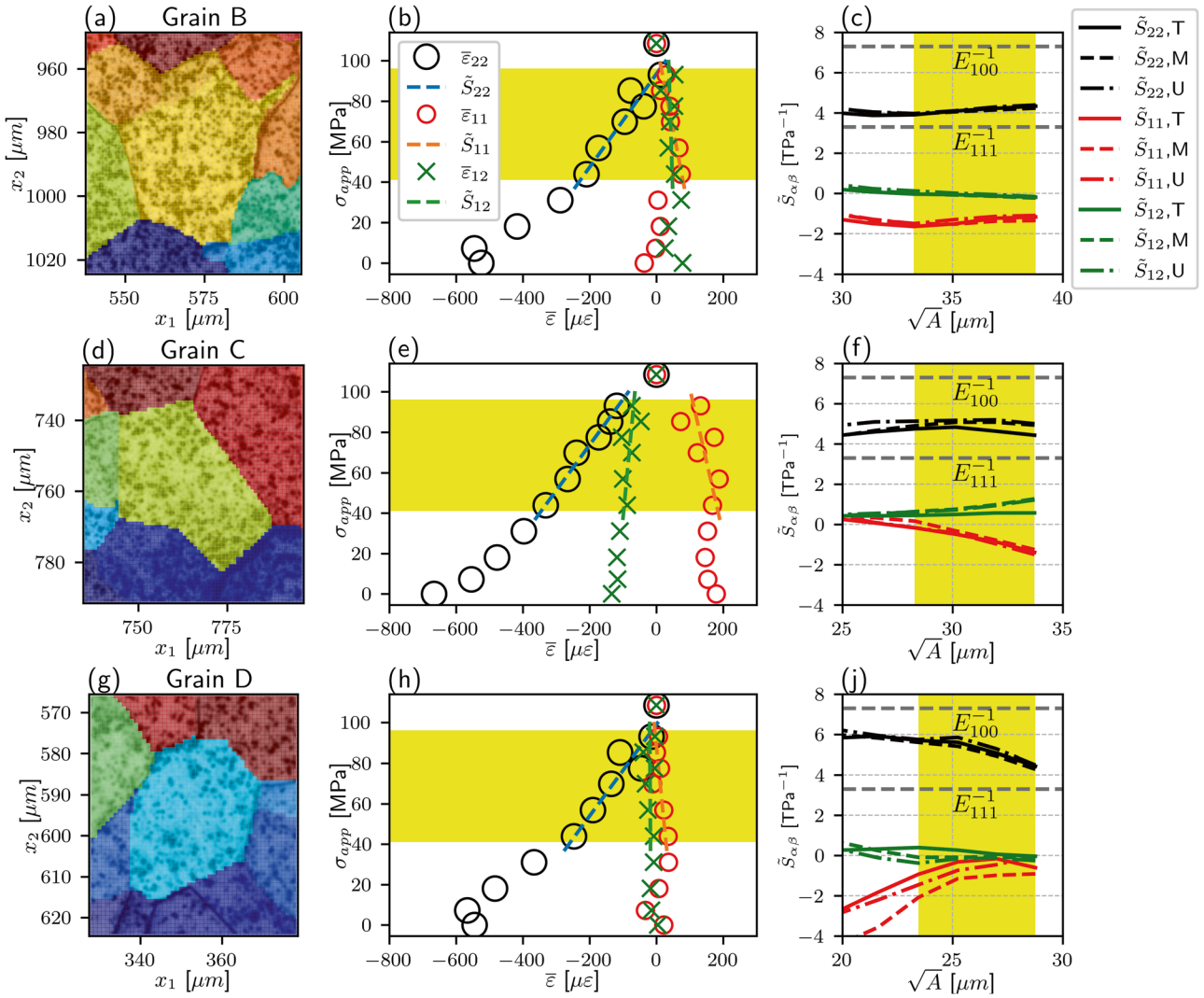

Fig. 7 For grain B, (**a**) image-grain mask overlay (grain B at center) at reference point T, (**b**) grain-averaged strain components over the unload, (**c**) calculated stress slopes $\tilde{S}_{\alpha\beta}$; (**d**), (**e**), (**f**) similarly for grain C; (**g**), (**h**), (**j**) similarly for grain D. For more details, see the caption of Fig. 6

$\tilde{S}_{22}$ paired with isostress-$\tilde{S}_{22}$ in Fig. 11(a), i.e., RMS-difference between experiment and model data points in Figs. 9(a) and 11(a) are 1.38 and 1.71 TPa^{-1}, respectively. In the direct comparison between spectral analysis and isostress predictions [Fig. 11(b)], the RMS-difference is 0.98 TPa^{-1}, but the more important distinction is the spread of the compliances and how much the spectral analysis regulates them into a narrow band. [For establishing another reference, note the isostrain (Taylor) assumption that would regulate the compliances into a single value (a band of zero thickness)].

The perceived overregulation of spectral analysis seems to play a part in the data cloud to be rotated vertically in Fig. 9(a). Among experimental $\tilde{S}_{\alpha\beta}$, there is higher confidence on $\tilde{S}_{22}$ with the highest signal. The average (with the proper grain area weighting) $\tilde{S}_{22}$ of the data cluster in Fig. 9(a) is found to be 4.1 TPa^{-1} which is in good agreement with the compliance of the bulk ("Aggregate Average" section; 1/240 GPa = 4.17 TPa^{-1}) In Fig. 9(a), multiple data points clustered about 2-3 and 6-7 TPa^{-1} ranges seem to corroborate a larger span of apparent compliance in actual fields compared to the spectral model.

The overregulation of the spectral analysis likely factors into the experiment-model comparison in Figs. 9(b, c) and 10(b, c) as well. Regardless though, the dispersion of the experimental data is clearly worse in the transverse components, $\tilde{S}_{11}$ and $\bar{\sigma}_{11}^{TU'}$. Area-weighted average of these yield − 2.75 TPa^{-1} and -38 MPa, respectively; and neither really check out against the bulk behavior, the former yielding an effective Poisson's ratio of about 0.65 ($\neq$ 0.33) and the latter not coming close to the ideal 0 (equations (1) and (7)). On the other hand, $\tilde{S}_{12}$ and $\bar{\sigma}_{12}$, both with ideal bulk values of zero, fare

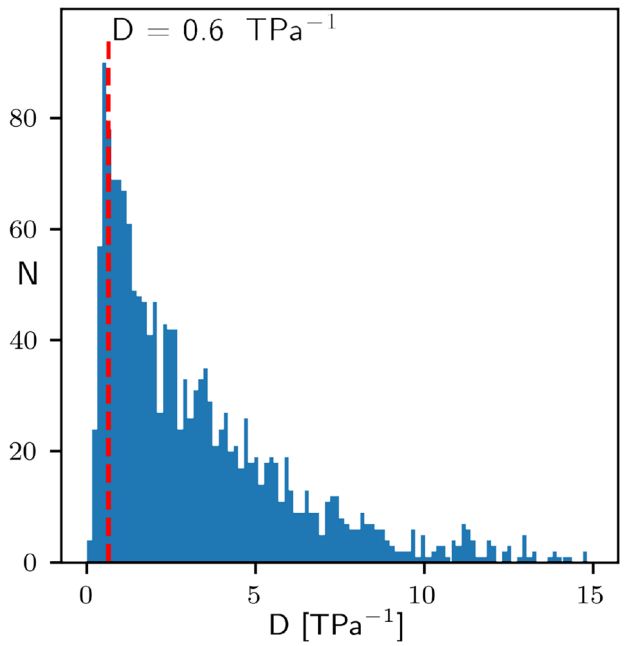

Fig. 8 Reference point discrepancy, D (equation (10)), root-mean-square of $\delta\tilde{S}_{\alpha\beta}$ over its independent calculations with different reference points and limited field erosions)

considerably better on their area-weighted averages, −0.44 TPa^{-1} and −5.5 MPa, each roughly an order below the corresponding axial values.

Though $\overline{\sigma}_{22}^{TU'}$ results will incur error from all stress slopes (including $\tilde{S}_{11}$), they also largely present bulk sanity, with an area-weighted average (87 MPa) within ∼ 20% of the nominal stress.

In summary, the statistics of grains that can satisfy the stringent accuracy requirement is limited. Obtaining accurate type-II results seems to be particularly testing in the transverse direction. In axial and shear components, the averages better satisfy the bulk sanity checks.

Discussion

On the Forecasted Application of the Idea

In this methodological effort, a single full unload has been considered. In a future application, multiple partial unloads (e.g., with a 30% reduction of σ_{app}) can be considered to continually estimate the type-II stress fields at numerous load points over the loading curve. In this scheme, right after each partial unload over which DIC data is collected, the sample is reloaded back to the flow curve. The operating assumption is that, over a sufficiently limited partial unload/reload, the strains released/recovered are virtually elastic.

This type of measurement emulates a grain-resolved diffraction instrument next to the DIC instrument [e.g., imagine a neighboring line in Fig. 2(a)] such that, at each *in situ* load point, the sample is transferred under the diffraction line to get grain-averaged stresses. Hence, type-II stress information is acquired over the very grains that are elucidated for type-III strain fields *in situ*.

The eventual benefit to the field is the potential for enhanced model validation. In comparison to validating a model with either strains or stress measures, a fundamental-scale constitutive model faces a sterner test when both are used. The fact that stresses are obtained at a coarser scale does not preclude a beneficial comparison, since a type-III model will easily allow proper averaging (as we do over the DAMASK output, see Supplementary Material) to meet the experimental data. The intense additional effort (grain maps, EBSD, additional measurement over unloads, etc.) is justified when the goal is the universal behavior of a metal.

Proof of Concept over Sporadic Grains

The large body of experimental and numerical work here, can still only be categorized as *progress* toward this

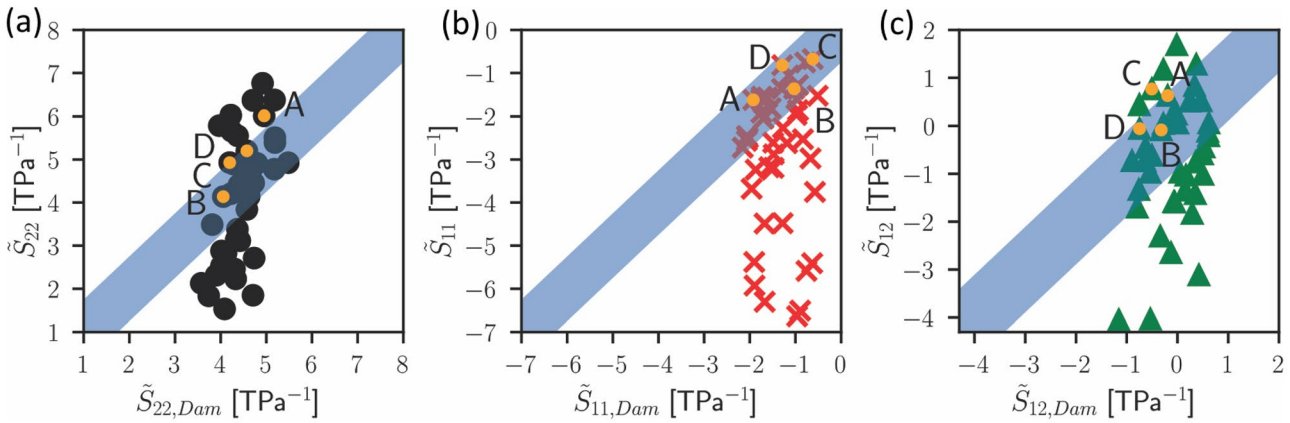

Fig. 9 Experimental grain-averaged stress slopes ($\tilde{S}_{\alpha\beta}$) versus spectral model (DAMASK) predictions ($\tilde{S}_{\alpha\beta,Dam}$) for (**a**) $\tilde{S}_{22}$, (**b**) $\tilde{S}_{11}$, and (**c**) $\tilde{S}_{12}$

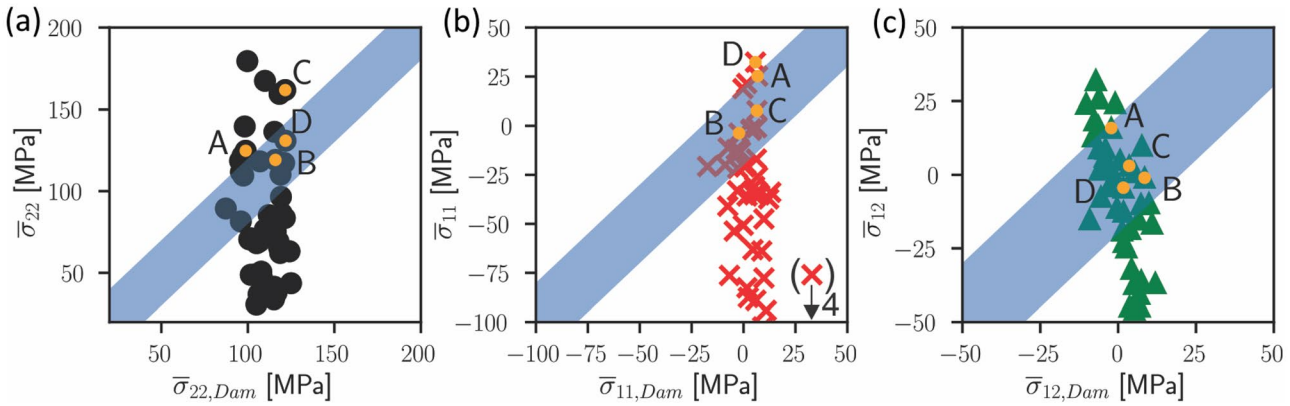

Fig. 10 For pre-unload point T, experimental grain-averaged stress ($\overline{\sigma}_{\alpha\beta}$) versus spectral model (DAMASK) predictions ($\overline{\sigma}_{\alpha\beta,Dam}$) for (**a**) $\overline{\sigma}_{22}^{TU'}$, (**b**) $\overline{\sigma}_{11}^{TU'}$, and (**c**) $\overline{\sigma}_{12}^{TU'}$. (See equation (5)) In part (**b**), 4 data points are below the shown range

ambitious idea. The fundamental difficulty is, clearly, squeezing elastic strain accuracy out of DIC (while retaining a degree of resolution). If objectivity (against RP variations) was considered for a variable that is in the standard reach of DIC, e.g., if strains were to be evaluated at an appreciable nominal plastic strain ($\sim 1\%$), and a maximum discrepancy of 1000 $\mu\varepsilon$ is sought for grain averages; virtually all grains in Fig. 8 would meet this condition—in contrast to the current outcome for elastic strain slopes.

Here, we have achieved proof-of-concept measurements on a limited number of grains ("Selected Individual Grain Evaluations" section). Given the demanding objective, this level of success would also not be possible without the meticulous preparation ("Material and Methods" section), but likely without the gross granular statistics. With the *physical conditions* of an objective (low D) multi-load-point elastic-strain-slope measurement rarely satisfied (Fig. 8, the large number of grains help in (the low-probability event of) getting good cases.

These *physical conditions* are necessarily sample and setup dependent. Recall the primary tenet of this micro-DIC setup in utilizing high-NA (low DOF = 1.6 μm) objectives with continual working distance maintenance through Z-corrections. (Over the full unload from point T to U, all frames show a consistent correction with $\Delta Z = 13.5 \pm 1\ \mu m$, with a nominally linear trend over the intermediate points, and the sense of the correction consistent with the compensated Poisson effect. Note, even over this predominantly elastic deformation, the Z-corrections are absolutely necessary to avoid defocusing.) These Z-corrections are conducted per frame (and not per grain). However, after metallography [Fig. 1(e)], the sample surface shows a degree of topography, i.e., the grains sit at slightly different elevations. This implies a variability in the accuracy of the WD for individual grains, leading to a variability in focus as well as incident light angles. We suppose that some grains (e.g., A-D) are better positioned; they tend to be consistently better focused when the frame is

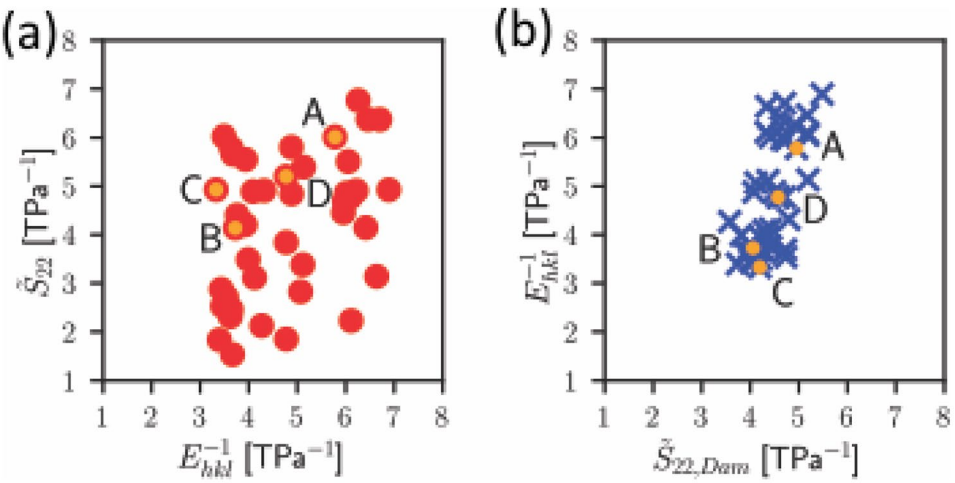

Fig. 11 Effective axial compliance comparisons, (**a**) experimental versus isostress value, (**b**) spectral model (DAMASK) versus isostress value

focused. Of course, the local DIC pattern quality—a generic variability source—is superposed over this factor.

Similar errors also exist when the targeted signal is plastic strains, but they tend to be quelled by ample signal. A brute-force amendment that can be offered for this setup is to record a fine Z-stack of images at each frame of each load, rather than the current procedure of recording one final image at Z_{foc}. Then, the image pair that is best for *each* grain in the reference and target Z-stacks could be explored.

Regarding the signal level, finally note that the current material choice has been a most challenging one with low strength (about 100 MPa, a pure metal) and high stiffness. If an alloy with similar stiffness but factors higher strength is considered, the partial unload stress and the resulting elastic strain signal can be scaled up [5, 25, 47].

Strain Heterogeneity

Let us first distinguish the actual elastic compliance of a grain S_{22} versus its apparent compliance, $\tilde{S}_{22}$, defined in equation (8)—constraining the arguments to axial components for brevity. S_{22} only depends on grain orientation; two grains in the aggregate with the same orientation, but with different morphology and different(-stiffness) neighbors, have the same S_{22}. These two grains, however, will clearly not have the same elastic strains and $\tilde{S}_{22}$, which is the σ_{app} slope of the elastic strains. The neighbors will affect the actual load/strain-partitioning [48], and the local morphology influences the fields. Note, such arguments hold in a purely elastic setting as well [48], before plasticity complicates the load partitioning.

Different zones in a grain, like the $\sqrt{A} = 32.1\ \mu m$ core of grain A [the third image in Fig. 6(l)] compared to its entire domain, are similar in that, while the two zones have the same orientation and S_{22}, they are averaged over a heterogeneous variation, leading to different $\tilde{S}_{22}$ values [see Fig. 6(l)].

The implemented consecutive-zones idea [Fig. 6(j–n)] also emphasizes that averaging zones are user-selected over DIC fields, which can spawn new ideas. In contrast, with diffraction applications with spot size larger than the grains, entire-grain-averaging is enforced at the signal level. Note, intragranular (type-III) strain heterogeneity necessarily exists in those measurements as well. In general, mechanical field averages over crystallites are never over constant fields [49, 50].

SEM-DIC applications, with possible 1-2 orders higher data density, have a distinct advantage in elucidating the intragranular fields [4, 7, 24]. Consequently, the idea of grain-averaged stress estimates can possibly be upgraded to coarse-intragranular resolution stress fields.

Complementary Modeling

Here, we discuss (i) the adequacy level of the spectral analysis, (ii) pointers on how these measurements can be used to complement full-field crystal plasticiy models.

Normally, of course, the measurement is supposed to validate modeling and not the other way around. For a type-II diffraction stress measurement as well [18], a physically exact simulation that validates the measurement does not, in general, exist. This stems not only from the adequacy of the model but an inherent lack of information about the aggregate. Note, e.g., the (typical [8]) unknown *sub*surface morphology of grains in this study. Accordingly, the spectral analysis with assumed columnar grains (see Supplementary Material) is only employed here to provide sanity checks. One should note the discord between the periodicity assumption of a spectral model and the actual traction-free boundary conditions of the surface measurement. (The difficult *surface effect* is at times specifically considered in the literature [51].) The third direction stresses are locally zero on the actual surface, whereas they are on-average zero in the spectral model. This is likely related to the *overregulation* of the spectral analysis results noted in "Statistics" section.

In a future application with model validation, the full-field simulation should rigorously incorporate the surface boundary conditions [8]. We remind that one needs to append unload steps to the model to deduce $\tilde{S}_{\alpha\beta}$ and the linearly-related $\overline{\sigma}^{TU'}_{\alpha\beta}$. If there is more confidence in $\tilde{S}_{22}$ compared to $\tilde{S}_{11}$ (as in "Statistics" section), the model can be made to meet only $\tilde{S}_{22}$, still retaining a degree of validation potential.

On the Stress Formalism

It would be desirable if the idea could access the stress at the point of interest on the loading curve, $\overline{\sigma}^{T}_{\alpha\beta}$, directly. Instead, (under the assumption of a linear elastic unload in a certain range), it measures $\overline{\sigma}^{TU'}_{\alpha\beta} = \overline{\sigma}^{T}_{\alpha\beta} - \overline{\sigma}^{U'}_{\alpha\beta}$. $\overline{\sigma}^{U'}_{\alpha\beta}$ is described as the stress state of the grain after the entire aggregate is unloaded over a hypothesized full elastic unload.

To elaborate, consider the microscopic internal state (dislocations, point defects, etc.) of the aggregate at the point of interest T. An elastic unload implies that this state is preserved, and only interatomic distances are altered upon unload. Once reverse plasticity starts, the microscopic state is not preserved, and the real unload point U (Fig. 3) has type-II residual stresses (granular stresses with zero sum) that corresponds to the altered microscopic state. However, a stress measurement that is purely associated with the load point over the flow curve (T) should not depend on the manner and extent of reverse plasticity in the event that a full

unload is implemented from this point. In fact, full unloads are not mandatory in the application of the idea ("On the Forecasted Application of the Idea" section).

Hence, it stands to reason that we are not measuring $\overline{\sigma}^{TU}_{\alpha\beta}$, but how can we naturally interpret $\overline{\sigma}^{TU'}_{\alpha\beta}$ and, for that purpose, the ground state $\overline{\sigma}^{U'}_{\alpha\beta}$? Take the nonelastic (in this case, plastic) strains of microscopic state T. Consider these being inserted to the maiden aggregate as an eigenstrain field. At zero far-field stress, this defines a residual stress field that is precisely $\overline{\sigma}^{U'}_{\alpha\beta}$ (since full elastic unload also means preserving the microscopic state down to zero far-field stress). So, $\overline{\sigma}^{U'}_{\alpha\beta}$ are the type-II (grain-averaged) residual stresses that correspond to the microscopic state of point T.

This undesirable complication (that granular measurements are baselined with $\overline{\sigma}^{U'}_{\alpha\beta}$) is inherently linked to the available information for stress. That ultimately is the load cell signal, only providing aggregate-average values, σ^{T}_{app}, which our formalism is based on (equations (4)–(6)). Nevertheless, $\tilde{S}_{\alpha\beta}$ (or alternatively $\overline{\sigma}^{TU'}_{\alpha\beta}$) are variables that are perfectly comparable between crystal plasticity models and experiments. Further, once validated, the model complements the absolute stress state of the grain at T, $\overline{\sigma}^{T}_{\alpha\beta}$.

Conclusion

The premise of deducing grain-specific stress information from total strain measurements over a polycrystal is explored in this study. To our best knowledge, this idea has been explored for the first time in this form and has three legs:

(i) A limited unload is functionally employed to extract elastic strain information. This assumes the entire polycrystal remains virtually elastic in this increment.
(ii) A formalism is posed to link this information to the stresses at the point of unload. The formalism requires the grain orientation and the crystal stiffness constants of the material.
(iii) The insufficient local accuracy of DIC (for assessing elastic strains) is improved by over-the-grain averaging.

This required additional facilities to be developed over the routine application of area-scanning micro-DIC:

(i) Highly accurate grain masks are produced that allows retrieving grain-specific information from the measured fields. Codes are developed to map the grain mask at one load to other load points.
(ii) Large-field EBSD is performed to get the orientation information for the identical grains studied by micro-DIC.
(iii) Micro-DIC data is *in situ* collected at multiple data points over the unload to evaluate the linearity of the response.

For evaluating the viability of the extremely subtle strains, internal sanity checks are developed:

(i) Conducting DIC with respect to multiple reference loads and checking their consistency.
(ii) Controlled stripping of the specific grain field to inspect stability of the results over the outer layers.

Few grains qualified over the fields by these measures for the very subtle quantity of elastic strain slopes. However, these provided sensible linear trends over loads, and provided sane values for strain slopes as well as stress estimates. Hence, with extremely careful implementations of microscopic DIC with high *intragranular* resolution, the premise of measuring *intergranular* stress measures via partial unloads seems to be viable and worthy of further exploration and verification. This capability that is superposed over strain measurement promises enhanced validation of crystal plasticity models.

Appendix. Stiffness Operator

The plane-stress linear elastic operator $\mathbf{C}^{\mathbf{g}}$ takes $(\varepsilon_{11}, \varepsilon_{22}, \varepsilon_{12})$ and outputs $(\sigma_{11}, \sigma_{22}, \sigma_{12})$. It corresponds to the solution of

$$\begin{bmatrix} \sigma_{11} \\ \sigma_{22} \\ 0 \\ 0 \\ 0 \\ \sigma_{12} \end{bmatrix} = \begin{bmatrix} C_{11} & C_{12} & C_{13} & C_{14} & C_{15} & C_{16} \\ C_{21} & C_{22} & C_{23} & C_{24} & C_{25} & C_{26} \\ C_{31} & C_{32} & C_{33} & C_{34} & C_{35} & C_{36} \\ C_{41} & C_{42} & C_{43} & C_{44} & C_{45} & C_{46} \\ C_{51} & C_{52} & C_{53} & C_{54} & C_{55} & C_{56} \\ C_{61} & C_{62} & C_{63} & C_{64} & C_{65} & C_{66} \end{bmatrix} \begin{bmatrix} \varepsilon_{11} \\ \varepsilon_{22} \\ * \\ * \\ * \\ 2\varepsilon_{12} \end{bmatrix}$$

where surface boundary conditions $\sigma_{33} = \sigma_{23} = \sigma_{13} = 0$ are imposed and $C_{IJ} = C_{IJ}(\mathbf{g})$ are the stiffness coefficients of the particular orientation, $\mathbf{g}$, in Voigt notation [41]. These are contracted from a full-index change of basis operation

$$C_{ijkl} = g_{iI}\, g_{jJ}\, g_{kK}\, g_{lL}\, c_{IJKL}$$

where C_{ijkl} and c_{IJKL} are the components of the stiffness tensor in sample and crystal coordinates, respectively, and g_{ij} is the orientation matrix.

Supplementary Information The online version contains supplementary material available at https://doi.org/10.1007/s11340-024-01050-4.

Acknowledgements The authors acknowledge the gracious help of Yeşim Yalçın and Asst. Prof. Eda Aydoğan of METU, Department of Materials and Metallurgical Engineering, with EBSD measurements.

Funding Open access funding provided by the Scientific and Technological Research Council of Türkiye (TÜBİTAK). This research has in

part been supported by the B. U. Research Fund at Bogazici University under Contract No. 14A06P4.

Data Availability Data is available upon request.

Declarations

Conflict of Interest The authors declare that they have no conflict of interest.

Open Access This article is licensed under a Creative Commons Attribution 4.0 International License, which permits use, sharing, adaptation, distribution and reproduction in any medium or format, as long as you give appropriate credit to the original author(s) and the source, provide a link to the Creative Commons licence, and indicate if changes were made. The images or other third party material in this article are included in the article's Creative Commons licence, unless indicated otherwise in a credit line to the material. If material is not included in the article's Creative Commons licence and your intended use is not permitted by statutory regulation or exceeds the permitted use, you will need to obtain permission directly from the copyright holder. To view a copy of this licence, visit http://creativecommons.org/licenses/by/4.0/.

References

1. Grédiac M, Sur F, Blaysat B (2016) The grid method for in-plane displacement and strain measurement: a review and analysis. Strain 52:205–243. https://doi.org/10.1111/str.12182
2. Efstathiou C, Sehitoglu H, Lambros J (2010) Multiscale strain measurements of plastically deforming polycrystalline titanium: role of deformation heterogeneities. Int J Plast. https://doi.org/10.1016/j.ijplas.2009.04.006
3. Shafaghi N, Kapan E, Aydıner CC (2020) Cyclic strain heterogeneity and damage formation in rolled magnesium via *in situ* microscopic image correlation. Exp Mech. https://doi.org/10.1007/s11340-020-00612-6
4. Orozco-Caballero A et al (2017) How magnesium accommodates local deformation incompatibility: a high-resolution digital image correlation study. Acta Mater 133:367–379. https://doi.org/10.1016/j.actamat.2017.05.040
5. Stinville J-C et al (2016) Sub-grain scale digital image correlation by electron microscopy for polycrystalline materials during elastic and plastic deformation. Exp Mech 56:197–216. https://doi.org/10.1007/s11340-015-0083-4
6. Erman SC, Stainier L, Aydıner CC (2023) Guiding severely anisotropic twinning bands in Magnesium: an *in situ* investigation by full-field microscopic image correlation. Mater Today Commun. https://doi.org/10.1016/j.mtcomm.2023.106203
7. Yaghoobi M et al (2022) Deformation twinning and detwinning in extruded Mg-4Al: *in-situ* experiment and crystal plasticity simulation. Int J Plast 155:103345. https://doi.org/10.1016/j.ijplas.2022.103345
8. Githens A et al (2020) Characterizing microscale deformation mechanisms and macroscopic tensile properties of a high strength magnesium rare-earth alloy: a combined experimental and crystal plasticity approach. Acta Mater 186:77–94. https://doi.org/10.1016/j.actamat.2019.12.012
9. Lim H et al (2014) Grain-scale experimental validation of crystal plasticity finite element simulations of tantalum oligocrystals. Int J Plast 60:1–18. https://doi.org/10.1016/j.ijplas.2014.05.004
10. Guan Y et al (2017) Crystal plasticity modelling and HR-DIC measurement of slip activation and strain localization in single and oligo-crystal Ni alloys under fatigue. Int J Plast 88:70–88. https://doi.org/10.1016/j.ijplas.2016.10.001
11. Clausen B, Lorentzen T, Leffers T (1998) Self-consistent modelling of the plastic deformation of f.c.c. polycrystals and its implications for diffraction measurements of internal stresses. Acta Mater 46:3087–3098. https://doi.org/10.1016/S1359-6454(98)00014-7
12. Abdolvand H, Daymond MR (2012) Internal strain and texture development during twinning: comparing neutron diffraction measurements with crystal plasticity finite-element approaches. Acta Mater 60:2240–2248. https://doi.org/10.1016/j.actamat.2012.01.016
13. Máthis K et al (2015) Effect of the loading mode on the evolution of the deformation mechanisms in randomly textured magnesium polycrystals - Comparison of experimental and modeling results. Int J Plast 72:127–150. https://doi.org/10.1016/j.ijplas.2015.05.009
14. Tari V et al (2018) Validation of micro-mechanical FFT-based simulations using high energy diffraction microscopy on Ti-7Al. Acta Mater 154:273–283. https://doi.org/10.1016/j.actamat.2018.05.036
15. Aydıner CC, Brown DW, Mara NA, Almer J, Misra A (2009) *In situ* x-ray investigation of freestanding nanoscale Cu-Nb multilayers under tensile load. Appl Phys Lett 94:031906. https://doi.org/10.1063/1.3074374
16. Turner T et al (2016) Combined near- and far-field high-energy diffraction microscopy dataset for Ti-7Al tensile specimen elastically loaded *in situ*. Integr Mater Manuf Innov. https://doi.org/10.1186/s40192-016-0048-1
17. Oddershede J et al (2011) Grain-resolved elastic strains in deformed copper measured by three-dimensional x-ray diffraction. Mater Charact 62:651–660. https://doi.org/10.1016/j.matchar.2011.04.020
18. Aydıner CC et al (2009) Evolution of stress in individual grains and twins in a magnesium alloy aggregate. Phys Rev B. https://doi.org/10.1103/PhysRevB.80.024113
19. Tamura N et al (2003) Scanning X-ray microdiffraction with submicrometer white beam for strain/stress and orientation mapping in thin films. J Synchrotron Radiat 10:137–143. https://doi.org/10.1107/S0909049502021362
20. Jakobsen B, Poulsen HF, Lienert U, Pantleon W (2007) Direct determination of elastic strains and dislocation densities in individual subgrains in deformation structures. Acta Mater 55:3421–3430. https://doi.org/10.1016/j.actamat.2007.01.049
21. Plancher E et al (2019) Validity of crystal plasticity models near grain boundaries: contribution of elastic strain measurements at micron scale. JOM 71:3543–3551. https://doi.org/10.1007/s11837-019-03711-5
22. Özdür NA, Üçel IB, Yang J, Aydıner CC (2020) Residual intensity as a morphological identifier of twinning fields in microscopic image correlation. Exp Mech. https://doi.org/10.1007/s11340-020-00672-8
23. Abuzaid WZ, Sangid MD, Carroll JD, Sehitoglu H, Lambros J (2012) Slip transfer and plastic strain accumulation across grain boundaries in Hastelloy X. J Mech Phys Solids 60:1201–1220. https://doi.org/10.1016/j.jmps.2012.02.001
24. Di Gioacchino F, Quinta Da Fonseca J (2015) An experimental study of the polycrystalline plasticity of austenitic stainless steel. Int J Plast 74:92–109. https://doi.org/10.1016/j.ijplas.2015.05.012
25. Stinville J et al (2020) Measurement of elastic and rotation fields during irreversible deformation using Heaviside-digital image correlation. Mater Charact 169:110600. https://doi.org/10.1016/j.matchar.2020.110600
26. Kapan E, Shafaghi N, Uçar S, Aydıner CC (2017) Texture-dependent character of strain heterogeneity in magnesium az31 under reversed loading. Mater Sci Eng, A 684:706–711. https://doi.org/10.1016/j.msea.2016.12.085
27. Carroll J, Abuzaid W, Lambros J, Sehitoglu H (2010) An experimental methodology to relate local strain to microstructural texture. Rev Sci Instrum 81:83703. https://doi.org/10.1063/1.3474902
28. Field DP (1997) Recent advances in the application of orientation imaging. Ultramicroscopy 67:1–9. https://doi.org/10.1016/S0304-3991(96)00104-0

29. English AT, Chin GY (1965) On the variation of wire texture with stacking fault energy in f.c.c. metals and alloys. Acta Metall 13:1013–1016
30. Telemez MA, Aydıner CC (2014) Multiscale deformation heterogeneity in twinning magnesium investigated with *in situ* image correlation. Int J Plast. https://doi.org/10.1016/j.ijplas.2013.12.001
31. Üçel İB, Kapan E, Türkoğlu O, Aydıner CC (2019) *In situ* investigation of strain heterogeneity and microstructural shear bands in rolled magnesium AZ31. Int J Plast. https://doi.org/10.1016/j.ijplas.2019.02.008
32. Preibisch S, Saalfeld S, Tomancak P (2009) Globally optimal stitching of tiled 3D microscopic image acquisitions. Bioinformatics 25:1463–1465. https://doi.org/10.1093/bioinformatics/btp184
33. Rueden CT et al (2017) Image J2: imageJ for the next generation of scientific image data. BMC Bioinformatics 18:529. https://doi.org/10.1186/s12859-017-1934-z
34. Geusebroek JM, Cornelissen F, Smeulders AW, Geerts H (2000) Robust autofocusing in microscopy. Cytometry 39:1–9. https://doi.org/10.1002/(SICI)1097-0320(20000101)39:1<1::AID-CYTO2>3.0.CO;2-J
35. Guizar-Sicairos M, Thurman ST, Fienup JR (2008) Efficient subpixel image registration algorithms. Opt Lett 33:156. https://doi.org/10.1364/OL.33.000156
36. Pan B, Li K, Tong W (2013) Fast, robust and accurate digital image correlation calculation without redundant computations. Exp Mech 53:1277–1289. https://doi.org/10.1007/s11340-013-9717-6
37. Pan B (2007) Full-field strain measurement using a two-dimensional Savitzky-Golay digital differentiator in digital image correlation. Opt Eng 46:033601. https://doi.org/10.1117/1.2714926
38. Haddadi H, Belhabib S (2008) Use of rigid-body motion for the investigation and estimation of the measurement errors related to digital image correlation technique. Opt Lasers Eng 46:185–196. https://linkinghub.elsevier.com/retrieve/pii/S0143816607001029
39. Bradsk G (2000) The OpenCV library. Dr. Dobb's Journal of Software Tools
40. Collaboration Astropy et al (2022) The astropy project: sustaining and growing a community-oriented open-source project and the latest major release (v5.0) of the core package. Applied Journal of Physics 935:167. https://doi.org/10.3847/1538-4357/ac7c74
41. Freund LB, Suresh S (2004) Thin film materials. Cambridge University Press. https://doi.org/10.1017/CBO9780511754715
42. Roters F et al (2019) DAMASK - The Düsseldorf Advanced Material Simulation Kit for modeling multi-physics crystal plasticity, thermal, and damage phenomena from the single crystal up to the component scale. Comput Mater Sci 158:420–478. https://doi.org/10.1016/j.commatsci.2018.04.030
43. Groeber MA, Jackson MA (2014) Dream.3d: a digital representation environment for the analysis of microstructure in 3D. Integr Mater Manuf Innov. https://doi.org/10.1186/2193-9772-3-5
44. Sachs G (1928) Zur ableitung einer fliessbedingung. Z Ver Dtsch Ing 72:734–736
45. Hunter JD (2007) Matplotlib: a 2D graphics environment. Comput Sci Eng 9:90–95. https://doi.org/10.1109/MCSE.2007.55
46. Virtanen P et al (2020) SciPy 1.0: fundamental algorithms for scientific computing in Python. Nat Methods 17:261–272
47. Latypov MI et al (2021) Insight into microstructure-sensitive elastic strain concentrations from integrated computational modeling and digital image correlation. Scripta Mater 192:78–82. https://doi.org/10.1016/j.scriptamat.2020.10.001
48. Bretin R, Levesque M, Bocher P (2019) Neighborhood effect on the strain distribution in linearly elastic polycrystals: part 1 - Finite element study of the interaction between grains. Int J Solids Struct 176–177:36–48. https://doi.org/10.1016/j.ijsolstr.2019.05.015
49. Wejdemann C, Lienert U, Pantleon W (2010) Reversal of asymmetry of X-ray peak profiles from individual grains during a strain path change. Scripta Mater 62:794–797. https://doi.org/10.1016/j.scriptamat.2010.01.032
50. Obstalecki M, Wong SL, Dawson PR, Miller MP (2014) Quantitative analysis of crystal scale deformation heterogeneity during cyclic plasticity using high-energy x-ray diffraction and finite-element simulation. Acta Mater 75:259–272. https://doi.org/10.1016/j.actamat.2014.04.059
51. Diehl M, Shanthraj P, Eisenlohr P, Roters F (2015) Neighborhood influences on stress and strain partitioning in dual-phase microstructures: an investigation on synthetic polycrystals with a robust spectral-based numerical method. Meccanica 51:429–441. https://doi.org/10.1007/s11012-015-0281-2

Publisher's Note Springer Nature remains neutral with regard to jurisdictional claims in published maps and institutional affiliations.